PULSAR SCINTILLATION AND THE LOCAL BUBBLE

N. D. Ramesh Bhat, Yashwant Gupta, and A. Pramesh Rao
National Centre for Radio Astrophysics, TIFR, Post Bag 3, Ganeshkhind, Pune 411 007, India

ABSTRACT

We present the results from an extensive scintillation study of 20 pulsars in the dispersion measure range 3–35 pc cm^{-3}, carried out using the Ooty Radio Telescope at 327 MHz, to investigate the distribution of ionized material in the local interstellar medium (LISM). Observations were made during the period 1993 January–1995 August, in which the dynamic scintillation spectra of these pulsars were regularly monitored over 10–90 epochs spanning ~ 100 days. Reliable and accurate estimates of strengths of scattering have been deduced from the scintillation parameters, averaged out for their long-term fluctuations arising from refractive scintillation effects. Our analysis reveals several anomalies in the scattering strength, which suggest that the distribution of scattering material in the solar neighborhood is not uniform. We have modeled these anomalous scattering effects in terms of inhomogeneities in the distribution of electron density fluctuations in the LISM. Our model suggests the presence of a low-density bubble surrounded by a shell of much higher density fluctuations. We are able to put some constraints on geometrical and scattering properties of such a structure and find it to be morphologically similar to the Local Bubble known from other studies.

Subject headings: ISM: bubbles — ISM: general — ISM: structure — pulsars: general

1. INTRODUCTION

The solar system is believed to reside in a very hot (temperature $T \sim 10^6$ K) and tenuous (electron density $n_e \approx 0.005$ cm^{-3}) X-ray–emitting cavity, which is typical of the coronal phase of the interstellar medium (ISM) and is possibly produced by supernovae or winds from hot, massive stars (Cox & Reynolds 1987; McCammon & Sanders 1990). This region, often termed the Local Bubble, has been of considerable interest to both observers and theorists alike, owing to its proximity and atypical nature.

X-ray data reveal that the Local Bubble has an elongated geometry, extending up to 200–300 pc perpendicular to the Galactic plane and up to 50–100 pc in the plane (Snowden et al. 1990). This region was also noted for its deficiency of neutral hydrogen gas (Paresce 1984), and recent studies in the EUV band of a large sample of bright sources (Warwick et al. 1993) estimate the gas density to be ~ 0.05 cm^{-3}. The local interstellar medium (LISM), which consists of the bubble and its surroundings, has rather loose definitions (Cox & Reynolds 1987; Bochkarev 1987), and in this paper we use this term to mean a region of a few 100 pc surrounding us. Although adequate understanding exists to say that the LISM deviates significantly in its properties from the Galactic average, there are several aspects that lack satisfactory understanding, especially its detailed morphological characteristics, its accurate size, the nature of its boundary, and the properties of the material in it.

Propagation effects on radio waves emitted by pulsars, such as dispersion and scattering, probe the distribution of thermal plasma in the ISM. In particular, observable effects of the scattering of radio waves from pulsars enable us to probe the electron density fluctuations in the ISM (see Rickett 1990 for a review). These density fluctuations are thought to arise from turbulence, and, hence, scintillation studies of pulsars also provide information on the nature and distribution of the interstellar turbulence (Cordes, Weisberg, & Boriakoff 1985). The distribution of electron density fluctuations in the LISM can differ significantly from the typical ISM because of the Local Bubble. It is reasonable to expect the Local Bubble and its environment to play a substantial role in determining the scintillation properties of nearby (distance $\lesssim 1$ kpc) pulsars. Such pulsars, therefore, form potential tools for studying the LISM.

Pulsar scintillation properties are best studied using their dynamic spectra—records of intensity variations in the time-frequency plane—which show random intensity modulations that fade over narrow frequency ranges and short time intervals. The phenomenon giving rise to this effect, known as diffractive scintillation, arises from a scattering of pulsar signals by the small-scale (10^7 m $\lesssim s \lesssim 10^9$ m) density fluctuations present in the ISM (Rickett 1990; Cordes, Pidwerbetsky, & Lovelace 1986; Spangler 1988). The decorrelation bandwidth, i.e., the frequency range over which the intensity decorrelates, provides information on the strength of scattering along the line of sight. In addition, the average scintillation properties of pulsar dynamic spectra are also expected to show variations over timescales of days to weeks at meter wavelengths as a result of refractive scintillation effects (Cordes et al. 1986; Romani, Narayan, & Blandford 1986; Rickett 1990). These arise from propagation of pulsar signals through large-scale ($s \gtrsim 10^{11}$ m) density irregularities in the ISM. Therefore, estimates of average scintillation properties from a few epochs of observation of dynamic spectra are prone to errors due to refractive scintillation effects. A large number of long stretches of data taken over time spans of months to years are essential for getting reliable and accurate estimates of scintillation parameters. Systematic studies of this kind have not been carried out for many pulsars, and most earlier measurements were based on only a few epochs of observations.

Not much is known about the electron density distribution of the interstellar gas in the LISM. Current models predict uniform electron density and uniform electron density fluctuations, except for a smooth dependence with height above the Galactic plane (Taylor & Cordes 1993; Cordes et al. 1985). Recent scintillation observations of PSR

B0950+08 suggest that the interior of the bubble is dominated by relatively lower magnitudes of density fluctuations (Phillips & Clegg 1992). However, there has been no accurate and systematic study of the connection between scintillation properties of local pulsars and the structure of the LISM.

During 1993–1995 we carried out a long-term, systematic study of the scintillation properties of 20 nearby pulsars, with the twofold aim of (i) studying refractive scintillation effects and (ii) understanding the LISM. In this paper, we describe the results of the second study. The results of the first part are presented in another paper (Bhat, Rao, & Gupta 1998b). Our observations are described in § 2. In § 3 we present the results of the data analysis and discuss its implications for the distribution of electron density fluctuations in the LISM. In § 4 we discuss the viability of simple models of specific density structures in explaining the present observations. The success and limitations of our best model are briefed in § 5, where we also compare it with pertinent results from other published studies on the LISM. At the end, we suggest some possible tests for the present model and some useful observations that will improve upon the present understanding of the LISM.

2. OBSERVATIONS

Pulsar observations were made using the Ooty Radio Telescope (ORT), an equatorially mounted 530×30 m parabolic cylinder operating at 327 MHz (Swarup et al. 1971). The ORT has an effective collecting area of 8000 m^2 and a system temperature of 150 K, and it is sensitive to linearly polarized radiation with an electric field in the north-south plane. The telescope has $9\frac{1}{2}$ hr of hour-angle coverage and a declination coverage from $-55°$ to $+55°$. The ORT is a phased array, with 1056 dipoles at its feed, signals from which are combined to form the signals from north and south halves. These signals are input to a correlation spectrometer (Subramanian 1989) to yield the cross power spectrum of the signals from the north and south

halves. Pulsar data were taken over a bandwidth of 9 MHz. For pulsar scintillation observations, such spectra were obtained with 64 channels spanning the bandwidth, yielding a frequency resolution of ≈ 140 kHz. The data were acquired both on the pulse and also on part of the off-pulse regions of the pulsars. The data were calibrated for both the telescope gain and receiver bandpass, using a continuum source at a declination close to that of the pulsar being studied.

Within the sky coverage and the sensitivity limits of the ORT, there are 20 nearby pulsars that were found suitable for studying the LISM. These are listed in Table 1, along with relevant observational details. Here $N_{\rm ep}$ is the number of epochs of observations and $\Delta f_{\rm ch}$ and Δt are the frequency and time resolutions of the dynamic spectra. Leaving out some faint pulsars ($S_{400} \lesssim 25$ mJy) and a few short-period pulsars (period $\lesssim 100$ ms) that could not be observed because of our instrumental constraints, this list formed the complete sample of pulsars within a distance of $\lesssim 1$ kpc known at the time of our observations. Subsequently, more pulsars have been discovered, and there has been a considerable increase in the number of local pulsars. Our sample, despite its limited nature, has a sky coverage that is reasonably uniform (Fig. 4). The distance estimates of pulsars are given in column (3) of Table 1. We adopt distance estimates based on the model for electron density distribution given by Taylor & Cordes (1993). For two pulsars, PSR B0950+08 and PSR B0823+26, there are independent distance estimates from parallax measurements, and we adopt them in place of dispersion measure (DM) based distances.

The pulsars were observed for their dynamic scintillation spectra over a large number of epochs ($N_{\rm ep} \sim 10$–90), spanning ~ 100 days during 1993–1995. The number of epochs of observations and their separations were determined by their expected refractive scintillation properties. For the LISM studies, our basic aim was to obtain reliable estimates of the scintillation parameters by averaging out their

TABLE 1

PULSAR SAMPLE AND OBSERVING PARAMETERS

Pulsar (1)	DM (pc cm^{-3}) (2)	D (pc) (3)	l (deg) (4)	b (deg) (5)	Period of Observation (6)	$N_{\rm ep}$ (7)	$\Delta f_{\rm ch}$ (kHz) (8)	Δt (s) (9)
PSR B0031−07......	10.9	680	110	−70	1995 Apr–1995 Jul	2	140.60	9.43
PSR B0329+54......	26.8	1430	145	−1	1995 Apr–1995 Jul	14	140.60	7.15
PSR B0628−28......	34.4	2140	237	−17	1993 Oct–1994 Jan	17	140.60	12.44
PSR B0823+26......	19.5	380[a]	197	32	1993 Mar−1994 Jan	31	140.60[b]	13.27
PSR B0834+06......	12.9	720	220	26	1993 Jan–1995 Jul	93	140.60[b]	12.74
PSR B0919+06......	27.2	>2970	225	36	1994 Mar–1994 Jun	19	140.60	21.53
PSR B0950+08......	3.0	130[a]	229	44	1993 Oct−1995 Jul	3	281.20	12.65
PSR B1133+16......	4.8	270	242	69	1993 Feb–1995 Jul	59	140.60[b]	11.88
PSR B1237+25......	9.3	560	253	87	1993 Oct–1994 Jan	9	140.60	13.82
PSR B1508+55......	19.6	1930	91	52	1995 Apr–1995 Jul	9	140.60	14.79[c]
PSR B1540−06......	18.5	1160	1	37	1995 Apr–1995 Jul	12	140.60	14.18
PSR B1604−00......	10.7	590	11	36	1995 Apr–1995 Jul	10	140.60	21.09
PSR B1747−46......	21.7	1080	345	−10	1995 Apr–1995 Jul	12	140.60	14.85[c]
PSR B1919+21......	12.4	660	56	4	1993 Mar–1994 Jan	63	140.60[b]	13.37
PSR B1929+10......	3.2	170	47	−4	1994 Mar–1994 Jun	9	140.60	11.33
PSR B2016+28......	14.2	1100	68	−4	1993 Oct–1994 Jan	20	140.60	13.95
PSR B2020+28......	24.6	1300	69	−5	1994 Mar–1994 Jun	15	140.60	17.20[c]
PSR B2045−16......	11.5	640	31	−33	1993 Oct–1994 Jan	35	140.60	19.62
PSR B2310+42......	17.3	960	104	−16	1995 Apr–1995 Jul	10	140.60	17.47
PSR B2327−20......	8.4	490	49	−70	1994 Mar–1994 Jun	18	140.60	32.87

[a] Distance estimates from parallax method (Gwinn et al. 1986).
[b] Part of the data were taken with $\Delta f_{\rm ch} = 281.20$ kHz.
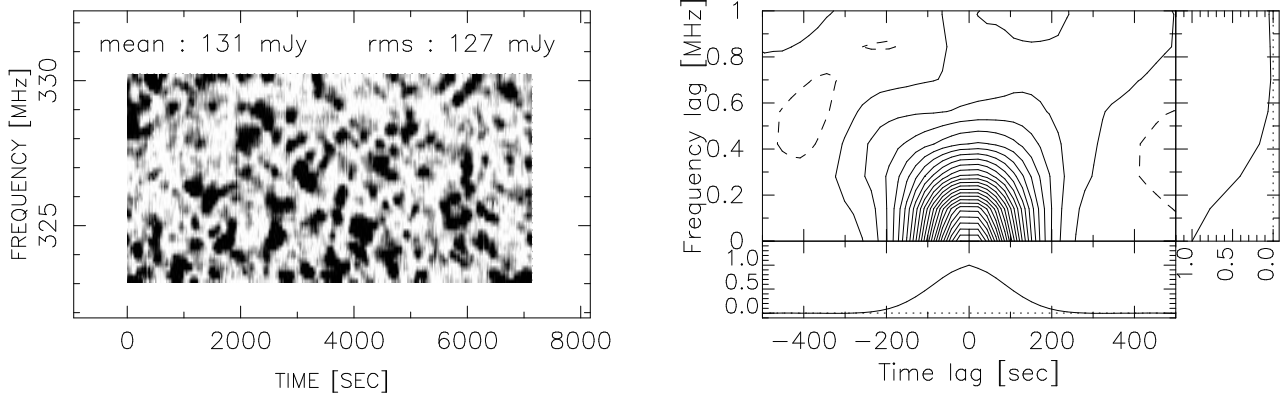[c] Part of the data were taken with larger Δt (twice the value given here).

FIG. 1.—Dynamic scintillation spectrum of PSR B0919+06 as observed on 1994 May 24, darker areas representing higher intensity values (*left*). The ACF is shown, along with one-dimensional cuts across zero lags of frequency and time (*right*).

fluctuations arising from refractive scintillation effects, which has been achieved except for two pulsars, PSR B0950+08 and PSR B0031−07. The pulsar PSR B0950+08 shows scintillation characteristics that were not measurable with our experimental setup (Fig. 2, *upper left*); in the case of PSR B0031−07, dynamic spectra observations turned out to be difficult because of the pulsar's nulling properties. At every epoch of observations, the
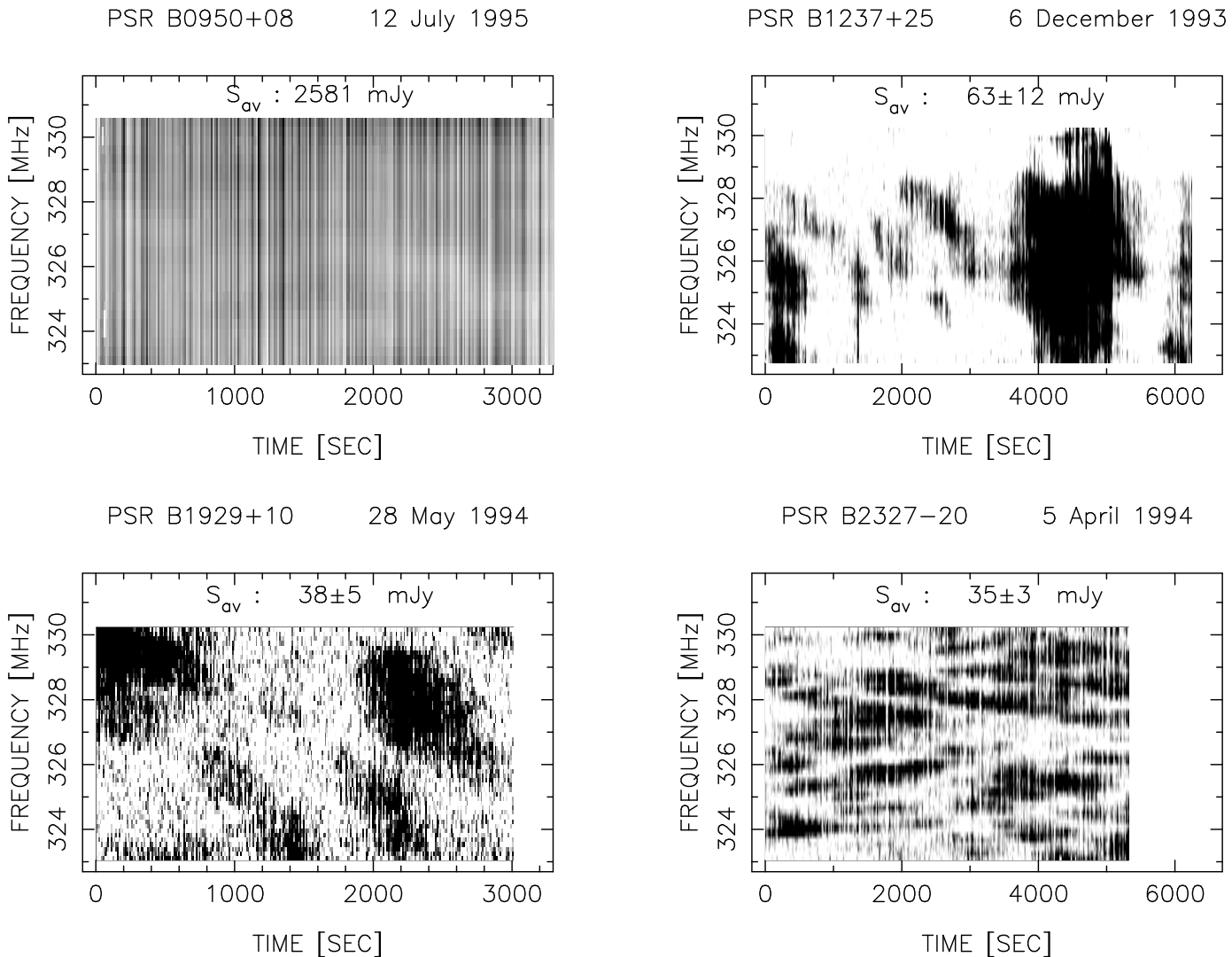

FIG. 2.—Sample dynamic spectra of four pulsars, shown to illustrate the wide range of scintillation properties of nearby pulsars. The darker areas represent higher intensity values. The white regions correspond to 20% of the mean intensity, and the black regions correspond to twice the mean intensity; in between, the intensity values are linearly represented by the gray scale. The apparent, temporal intensity fluctuations seen for the pulsar PSR B0950+08 are at about 25% level from the mean, which are likely to be intrinsic variations. S_{av} is the average flux as measured on the observing day given at the top of each panel.

dynamic spectrum of each pulsar was recorded over a typical duration of 2–3 hr in order to get accurate estimates of the scintillation characteristics. Further details regarding the observations and a description of our data analysis can be found in another paper (Bhat, Rao, & Gupta 1998a).

Figure 1 (*left*) shows a typical dynamic scintillation spectrum of pulsar PSR B0919+06, obtained from observations made on 1994 May 24. The intensity scintillation patterns of this pulsar decorrelate over ~ 100 s in time and ~ 250 kHz in frequency. Bright intensity regions, known as *scintles*, are resolvable when the instrumental resolutions in time and frequency happen to be smaller than respective decorrelation widths. With the frequency resolution available with our experimental setup ($\Delta f_{ch} \approx 140$ kHz), it is expected to resolve the spectral features of pulsars with DM < 40 pc cm^{-3} at our observing frequency. The required temporal resolution (Δt), typically ~ 10 s, is not a limiting factor, owing to the high sensitivity of the upgraded ORT (Selvanayagam et al. 1993). The pulsar data were integrated for ~ 10 s to average out the intrinsic pulse-to-pulse fluctuations of pulsar signals to an acceptable level. Our observations show that pulsar dynamic spectra vary significantly in their properties over timescales as short as 2–3 days, where the scintillation patterns change in terms of their sizes and shapes in the frequency-time plane.

Figure 2 displays sample dynamic spectra of some selected pulsars over DM range 3–10 pc cm^{-3}, illustrating the diversity and wide range in the scintillation characteristics of nearby pulsars. The spectra were obtained with $\Delta f_{ch} \approx 140$ kHz for pulsars PSR B1237+25, PSR B1929+10, and PSR B2327−20 and with $\Delta f_{ch} \approx 280$ kHz in the case of PSR B0950+08. The temporal resolutions are in the range of ~ 10–15 s. Figure 2 (*upper left*) displays the spectrum of PSR B0950+08, obtained from observations made on 1995 July 12. The scintillation patterns of this pulsar are not resolvable within our observing bandwidth and within typical observing durations of 2 hr, whereas the spectra of other pulsars show remarkable difference. In the case of PSR B2327−20 (Fig. 2, *lower right*), the patterns fade over a very narrow frequency range (~ 100 kHz). Pulsars PSR B1237+25 and PSR B1929+10 show this property over a much wider frequency range (~ 1 MHz; Fig. 2, *lower left and upper right*). Thus, the scintillation properties of local pulsars span a wide range of 2 orders of magnitude at our observing frequency.

3. DATA ANALYSIS AND RESULTS

3.1. *The Two-dimensional ACF Computation*

To quantify the average characteristics of the scintillation patterns at any epoch, we make use of the two-dimensional auto covariance function (2D ACF) technique. The ACF was computed for a maximum frequency lag of half the observing bandwidth and for a maximum time lag of half the observing time. The function was corrected for the effect of system noise fluctuations and the residual, intrinsic, pulse-to-pulse fluctuations, which, being uncorrelated, appear as a ridgelike feature at zero time lag in the 2D ACF. Figure 1 (*right*) shows such an ACF for PSR B0919+06 for the epoch 1994 May 24, where the display has been restricted to a maximum time lag of 500 s and a maximum frequency lag of 1 MHz. The 2D ACF can be characterized by its widths along zero frequency lag and zero time lag axes, which are the decorrelation bandwidth v_d (defined as

the half-maximum width along the zero time lag axis) and the scintillation time τ_d (defined as the e^{-1} width along the zero frequency lag axis). The 2D ACF was fitted with a two-dimensional Gaussian function of the following form:

$$\rho_k(v, \tau) = C_0 \exp\left[-(C_1 v^2 + C_2 v\tau + C_3 \tau^2)\right], \quad (1)$$

where v is the frequency lag and τ is the time lag. The suitability of this type of function in representing the ACF of a dynamic spectrum has been discussed by Gupta, Rickett, & Lyne (1994). The amplitude of the Gaussian function (C_0) is treated as unity in our case, since the computed ACF is normalized to unity amplitude. While carrying out the fitting, the deviations between the ACF and the model Gaussian are weighted by their uncertainties, which are essentially the estimates of rms noise and are determined from the noise in the dynamic spectrum and the number of data pairs averaged to get ρ_k.

The model parameters C_1, C_2, and C_3 are estimated by a χ^2 minimization procedure. The scintillation parameters v_d and τ_d can be expressed in terms of these model parameters as

$$v_d = \left(\frac{\ln 2}{C_1}\right)^{0.5}, \quad \tau_d = \left(\frac{1}{C_3}\right)^{0.5}. \quad (2)$$

The uncertainties in C_1 and C_3 are obtained from a χ^2 variation of unit magnitude from its minimum and translated into corresponding uncertainties in v_d and τ_d. We also take into account the estimation errors in v_d and τ_d arising because of a finite number of scintles, given by

$$\sigma_{est} = \left(\frac{B_{obs} t_{obs}}{v_d \tau_d}\right)^{-0.5}, \quad (3)$$

where σ_{est} is the fractional error, B_{obs} is the observing bandwidth, and t_{obs} is the duration over which the dynamic spectrum was recorded. Errors from the model fitting are added in quadrature with the estimation errors to get the final uncertainties in the parameters v_d and τ_d. The decorrelation widths obtained in this manner are corrected for smearing due to finite instrumental resolutions in frequency (Δf_{ch}) and in time (Δt), respectively. Barring a few exceptions, such as v_d measurements of pulsars PSR B1540−06 and PSR B2310+42 (Table 2), the instrumental smearing is not significant for our data. Our observations show large fluctuations of v_d and τ_d, and variations as large as a factor of 3–5 are seen for most pulsars. The typical rms fluctuations are about 40%–50%. Nevertheless, our large number of epochs of observations taken over time spans of ~ 100 days allow us to reduce the statistical uncertainties due to these fluctuations to about 5%–10% in the estimates of average scintillation parameters.

In order to get best estimates of average scintillation parameters from a given number of epochs of observations, we make use of a weighted average 2D ACF, which will be referred to as the global 2D ACF (GACF). It is obtained from our observations of dynamic spectra of the pulsar at all epochs, using the following definition:

$$\rho_g(v, \tau) = \frac{\sum_{k=1}^{k=N_{ep}'} \omega_k(v, \tau)\rho_k(v, \tau)}{\sum_{k=1}^{k=N_{ep}'} \omega_k(v, \tau)}, \quad (4)$$

where ρ_k is the ACF of a dynamic spectrum at the kth epoch. The value N_{ep}' is the number of epochs of observations made with identical resolutions in time and fre-

TABLE 2

MEASURED SCINTILLATION PARAMETERS AND $\overline{C_n^2}$ ESTIMATES

Pulsar (1)	$\nu_{d,g}$ (kHz) (2)	$\tau_{d,g}$ (s) (3)	log $\overline{C_n^2}$ (4)	log $\overline{C_n^2}$ (CWB)[a] (5)
PSR B0031−07......	1039 ± 208	2961 ± 592	−4.22 ± 0.058	...
PSR B0329+54......	165 ± 13	307 ± 25	−4.03 ± 0.024	−3.46
PSR B0628−28......	203 ± 18	455 ± 41	−4.54 ± 0.054	−4.48
PSR B0823+26......	293 ± 41	126 ± 19	−3.24 ± 0.025	−3.01
PSR B0834+06......	454 ± 27	390 ± 23	−3.91 ± 0.030	−3.33
PSR B0919+06......	256 ± 41	160 ± 27	−4.82 ± 0.023	−3.80
PSR B0950+08......	≫9000	>7500	≪−3.70	−2.91
PSR B1133+16......	816 ± 57	165 ± 12	−3.32 ± 0.052	−3.31
PSR B1237+25......	1828 ± 128	439 ± 26	−4.07 ± 0.085	−3.97
PSR B1508+55......	197 ± 33	158 ± 30	−4.40 ± 0.017	−4.13
PSR B1540−06......	111 ± 12	526 ± 58	−3.73 ± 0.026	...
PSR B1604−00......	378 ± 19	933 ± 56	−3.71 ± 0.057	−3.66
PSR B1747−46......	165 ± 21	215 ± 30	−3.85 ± 0.028	...
PSR B1919+21......	285 ± 14	374 ± 22	−3.95 ± 0.060	−2.84
PSR B1929+10......	1293 ± 78	348 ± 24	−3.13 ± 0.082	−2.94
PSR B2016+28......	206 ± 12	995 ± 60	−3.97 ± 0.053	−3.40
PSR B2020+28......	270 ± 22	279 ± 22	−4.10 ± 0.020	−3.74
PSR B2045−16......	539 ± 65	138 ± 17	−3.92 ± 0.018	−3.81
PSR B2310+42......	114 ± 15	309 ± 40	−3.46 ± 0.022	...
PSR B2327−20......	268 ± 11	432 ± 13	−3.41 ± 0.039	...

[a] Measurements of $\overline{C_n^2}$ from Cordes et al. 1985 corrected for the new pulsar distance estimates.

quency, and ω_k is the weight function, which is simply the number of data pairs averaged to get ρ_k. The GACFs computed in this manner are shown in Figure 3 for some pulsars. The signal-to-noise ratio in these ACFs is much higher than the individual ACFs, and this results in more reliable estimates of scintillation parameters. The GACF is fitted with a Gaussian of the form described in equation (1) to yield parameters $\nu_{d,g}$ and $\tau_{d,g}$, which are the average decorrelation bandwidth and the scintillation timescale, respectively. The values of $\nu_{d,g}$ and $\tau_{d,g}$ are presented in columns (2) and (3) of Table 2. In the case of PSR B0950+08, the GACF method does not give any meaningful results, since the pulsar has a decorrelation bandwidth much larger than our observing bandwidth ($\nu_d \gg 9$ MHz; see Fig. 2, *upper left*). This is consistent with the expectations based on its recent scintillation measurements at 50 MHz (Phillips & Clegg 1992).

Measurements of decorrelation bandwidth and scintillation time have been reported earlier by several groups (Roberts & Ables 1982; Cordes et al. 1985; Smith & Wright 1985; Cordes 1986; Gupta et al. 1994). A detailed comparison of the various measurements is discussed in our paper, describing in detail the ORT observations (Bhat et al. 1998a). There seem to be considerable unexplained discrepancies between the various measurements of decorrelation bandwidth (ν_d) and scintillation time (τ_d). Most earlier measurements were taken from fewer epochs of observations and, hence, are prone to errors due to refractive scintillation effects. On comparing our measurements with others, we find the differences to be more or less unbiased, except with those from Cordes et al. (1985). But we also note that measurements given in Cordes (1986) are from a more extensive data set and later than those reported in Cordes et al. (1985). If we restrict ourselves to these later measurements, by and large, there seems to be reasonable consistency between the various measurements, allowing for the fact that most earlier measurements did not take into consideration refractive scintillation effects. Since our measurements

are from long-term systematic observations, we have been able to obtain more reliable scintillation parameters by averaging out their refractive fluctuations. Therefore, we believe that ours are the most precise measurements made so far.

Among the two scintillation parameters discussed here, estimates of decorrelation bandwidths are better representatives of the strength of scattering. The timescales are determined by the coherence scales as well as the transverse speeds of pulsars. In the case of pulsars with low proper motions, the bulk motion of the medium and the Earth's orbital motion will also have substantial roles in determining the timescales. Furthermore, it is difficult to totally rule out intrinsic intensity variations of pulsars over timescales of the order of those due to interstellar scintillation (ISS). The timescales are, therefore, not as good indicators of strength of scattering as are the decorrelation bandwidths. We use estimates of $\nu_{d,g}$ to derive the strengths of scattering of our pulsars.

3.2. Estimation of Strength of Scattering

From the estimates of decorrelation bandwidths obtained by the aforementioned method, we deduce parameters characterizing the electron density fluctuations along the lines of sight of the observed pulsars. These density fluctuations are normally characterized by their power spectrum (see, for example, Rickett 1990), given by

$$P(\kappa) = C_n^2 \kappa^{-\alpha} \qquad \frac{2\pi}{s_o} \lesssim \kappa \lesssim \frac{2\pi}{s_i}, \qquad (5)$$

where κ is the spatial wavenumber and s_i and s_o are the inner and outer cutoffs of scale size, respectively. The amplitude of the spectrum C_n^2, which will be referred to as the strength of scattering in our discussion, is an indicator of the rms of electron density fluctuations. The measurable parameter decorrelation bandwidth is determined by the integral of C_n^2 over the line of sight. It is convenient to
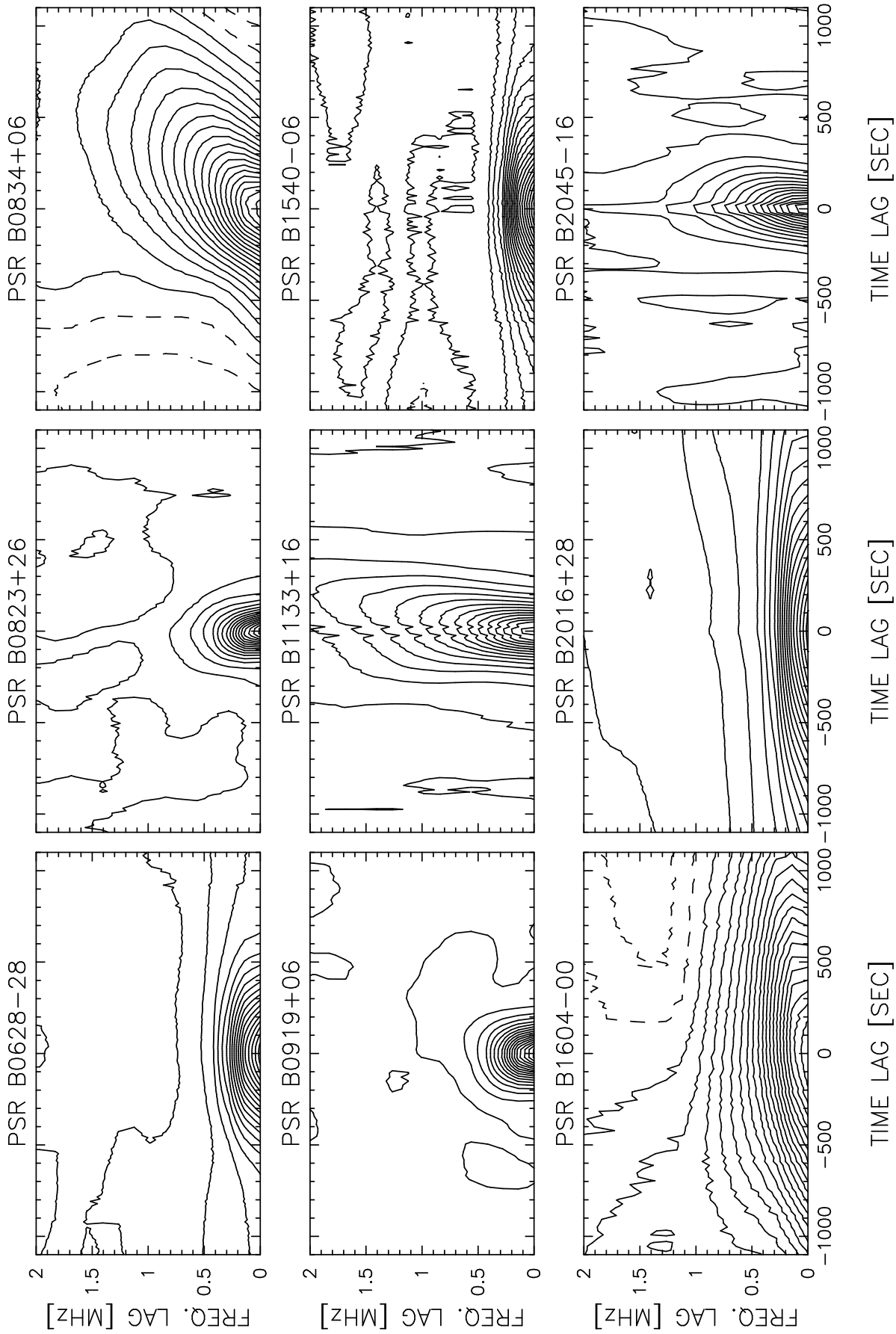
FIG. 3.—GACFs for some selected pulsars. These were computed from ∼ 10–30 independent ACFs. They represent the scintillation properties averaged over the entire time span of observations (see Table 1).

use a parameter $\overline{C_n^2}$, which is the line-of-sight–averaged value of C_n^2, to characterize the scattering from different directions. Cordes et al. (1985) have discussed in detail the estimation of $\overline{C_n^2}$, which is given by

$$\overline{C_n^2} = A_\alpha f_{\mathrm{obs}}^\alpha D^{-(\alpha/2)} v_d^{-[(\alpha-2)/2]}, \qquad (6)$$

where f_{obs} is the observing frequency in MHz, D is the distance estimate of the pulsar in parsecs, and A_α is a model-dependent constant. The value $\overline{C_n^2}$ is expressed in its standard units of $m^{-20/3}$. Armstrong, Rickett, & Spangler (1995) have shown that the electron density power spectrum in the local ($\lesssim 1$ kpc) ISM can be best represented by a power-law model, quite close to the Kolmogorov form. Therefore, we assume the Kolmogorov power-law index $\alpha = 11/3$ in our calculations. In this case, $A_\alpha = 2 \times 10^{-6}$ for the units used in our analysis. Our estimates of $\overline{C_n^2}$ are given in column (4) of Table 2. The uncertainties shown here are based on the error estimates of $v_{d,g}$ values. For a uniformly distributed scattering medium, $\overline{C_n^2}$ is expected to be a constant.

Our derived values of $\overline{C_n^2}$ (Table 2) show roughly 2 orders of magnitude fluctuations, ranging from $10^{-4.8\pm0.02}$ to $10^{-3.1\pm0.02}$ $m^{-20/3}$. For PSR B0950+08, we have only an upper limit on $\overline{C_n^2}$ ($\ll 10^{-3.7}$ $m^{-20/3}$) because of our observing bandwidth limitations. This is consistent with its recent scintillation measurements at 50 MHz (Phillips & Clegg 1992), where a value of $\approx 10^{-4.5\pm0.1}$ $m^{-20/3}$ was reported. Note that, for pulsars PSR B1747−46, PSR B2310+42, and PSR B2327−20, C_n^2 estimates have been obtained for the first time.

Cordes et al. (1985) measured $\overline{C_n^2}$ for 15 pulsars in our sample. Their results, however, differ considerably from those obtained from our observations. We find that, barring a few exceptions, their $\overline{C_n^2}$ values are, in general, larger than our values. Even after correcting their estimates for the new pulsar distances (Table 2), considerable discrepancy is seen for 10 pulsars. Reasonable agreement (within a difference of

10%–30%) is seen with five pulsars, whereas discrepancies ranging over 2–10 times are the case with the remaining ones, for which the revised estimates continue to be larger than ours. For pulsars PSR B0919+06 and PSR B1919+21, our estimates are about 10 times lower. In the case of PSR B0950+08, we only have an upper limit on $\overline{C_n^2}$, which is 6 times lower, and a much lower value (60 times) was reported by Phillips & Clegg (1992). Thus, the $\overline{C_n^2}$ measurements of Cordes et al. (1985) are, by and large, in disagreement with those from our observations. Since our $\overline{C_n^2}$ estimates have been derived using the measurements obtained from a large number of long stretches of data taken over time spans of the order of months to years, they are less prone to errors due to refractive scintillation effects. The v_d measurements used in our calculations are known with uncertainties as low as $\sim 5\%$–10%.

3.3. Distribution of $\overline{C_n^2}$ in the LISM

Cordes et al. (1988, 1991) studied the distribution of $\overline{C_n^2}$ in the Galaxy by combining scintillation measurements of a large number of pulsars and radio sources. The analysis of Cordes et al. (1988) revealed large fluctuations of $\overline{C_n^2}$ of several orders of magnitude, and the statistics vary strongly with Galactic latitude. Cordes et al. (1991) give a more refined distribution, but the details such as an additional inner Galaxy component are not relevant as far as the LISM is concerned. The empirical models given by them for the variation of the diffuse component of C_n^2 have an exponential distribution with z-height and a Gaussian in Galactocentric radius (eq. [6] of Cordes et al. 1988). According to their models, expected fluctuations over a region of $\lesssim 1$ kpc around the Sun is ~ 3–6 times, whereas our observations show much larger fluctuations, about two orders of magnitude. This implies that, even within the LISM, scattering material is rather nonuniformly distributed, and the empirical models given by Cordes et al. (1988, 1991) are too simplistic for the LISM.
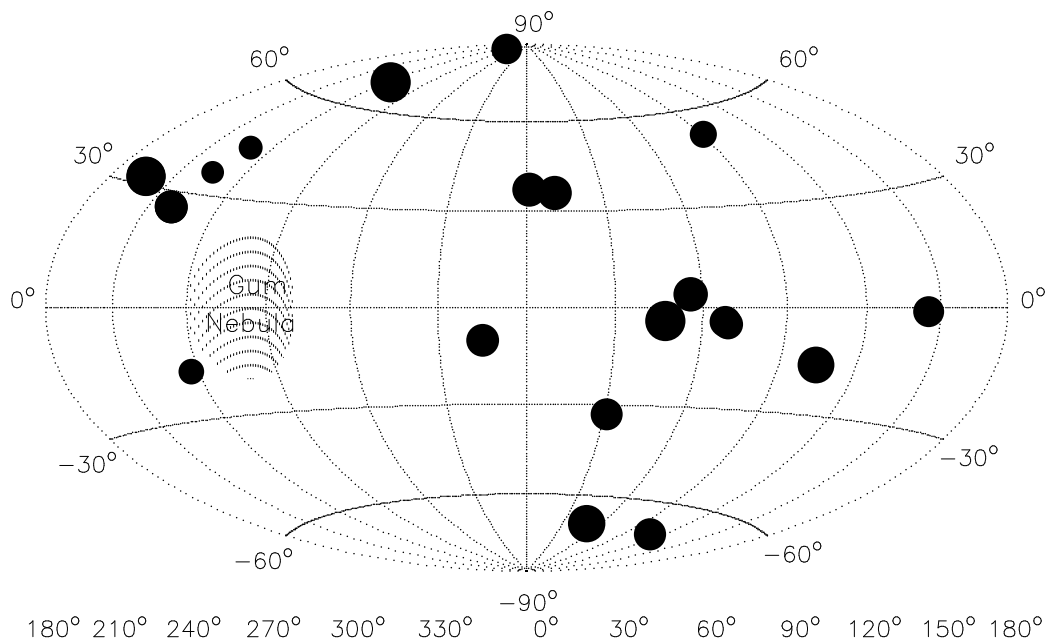

Fig. 4.—Sky distribution of $\overline{C_n^2}$ in the Galactic coordinate system, illustrating its observed fluctuations in the LISM. The size of the black circle represents log $\overline{C_n^2}$. The hatched region around ($l \approx 260°$, $b \approx 0°$) is the direction of the Gum Nebula, located at a distance of ~ 500 pc.

The observed fluctuations of our $\overline{C_n^2}$ measurements are shown in Figure 4. A complex distribution of this kind for the LISM has not been reported before. Our pulsar sample provides a fairly uniform coverage of the sky. Nevertheless, no large-scale trends are apparent for $\overline{C_n^2}(l, b)$, and there are no signatures of any clustering that are confined over a latitude or a longitude range. Also, note that our sample does not consist of any pulsar whose line of sight passes through the Gum Nebula; hence, there is no need to consider a possible enhancement of $\overline{C_n^2}$ because of the same.

Our estimates of $\overline{C_n^2}$ are plotted against pulsar distance estimates in Figure 5. A systematic trend is evident for the variation of $\overline{C_n^2}$ with distance. There are significant enhancements of $\overline{C_n^2}$ values within ~ 1 kpc surrounding the Sun, implying a probable local origin. Although a firm statement cannot be made, the $\overline{C_n^2}$ values appear to converge to a steady value at larger distances ($\gtrsim 2$ kpc).

The behavior of $\overline{C_n^2}$ with distance, DM, and (l, b) has been investigated earlier to understand the nature of distribution of turbulence in the Galaxy. Cordes et al. (1985) made $\overline{C_n^2}$ measurements of a large number of pulsars, and their data showed fluctuations as large as 5 orders of magnitude over DM range 3–475 pc cm^{-3} or distances up to ~ 10 kpc (Fig. 9 in Cordes et al. 1985). If we examine only those pulsars that are closer than 1 kpc (similar to our sample), these data also show a similar, though weaker, trend with distance. However, the effect was not noticed, since their emphasis was on studying large-scale Galactic distribution. The effect might have gotten further subdued, because their measurements were prone to errors due to refractive scintillation effects. Subsequent to Cordes et al. (1985), pulsar distances have been revised (Taylor & Cordes 1993). We have examined the above data with revised $\overline{C_n^2}$, and the weak trend remains unchanged. Since our estimates of $\overline{C_n^2}$ are obtained from more precise measurements of ν_d, where long-term refractive fluctuations have been averaged out, we see a more obvious trend in Figure 5.

To further assess the necessity of a nonuniform local scattering medium to explain the present observations, we studied the deviations of the present scintillation measurements relative to those expected from a uniform medium. We assumed a uniform medium with $\overline{C_n^2} \approx 0.2 \times 10^{-4}$ m$^{-20/3}$, which is the average of $\overline{C_n^2}$ of pulsars at ~ 2–3 kpc where the observed trend is closer to that of a uniform medium. The discrepancies between the observations and the expectations are shown in terms of ratios of decorrela-
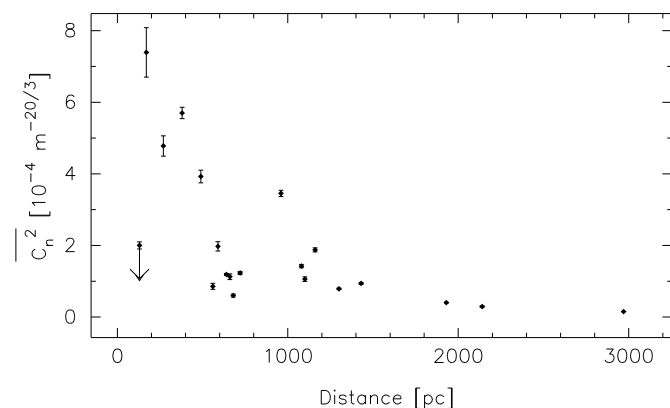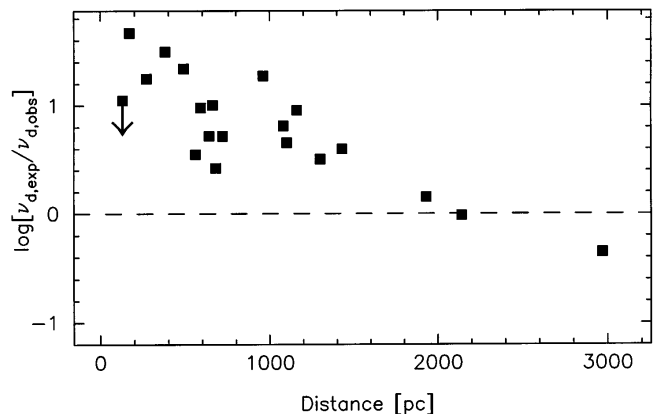

FIG. 6.—Deviations of the observed decorrelation bandwidth ($\nu_{d,\text{obs}}$) measurements from their values expected ($\nu_{d,\text{exp}}$) in the case of a uniform scattering medium with $\overline{C_n^2} \approx 0.2 \times 10^{-4}$ m$^{-20/3}$. The upper limit (*downward arrow*) is for PSR B0950+08.

tion bandwidths (Fig. 6). Observed measurements show considerable deviations from those due to a uniform medium, and a systematic trend with distance, similar to the case of $\overline{C_n^2}$, is seen. Most nearby pulsars show enhanced scattering relative to a uniform medium. The wide ranges and systematic trends of the observable ν_d and the derived parameter $\overline{C_n^2}$ suggest a nonuniform but organized distribution of scattering material in the LISM.

3.4. *Anomalies in Strengths of Scattering*

Our observations reveal several cases of pulsars with similar DMs or at similar distances showing remarkably different scintillation characteristics. Pulsars PSR B0950+08 and PSR B1929+10 form one of the prominent examples from our data (Fig. 2, *upper left and lower left*) where, despite having similar DMs and comparable distances (Table 1), their decorrelation bandwidths differ by 1–2 orders of magnitude. Such effects will be referred to as scattering anomalies in our discussion. Pulsars PSR B1237+25 and PSR B2327−20 are another example showing this property (Fig. 2, *upper right and lower right*), where, though they are of similar DMs, their decorrelation bandwidths differ by a factor of 4. In order to quantify such effects, we use the following method.

If we consider two pulsars such that their DMs differ by less than 10%, then their scattering strengths are also expected to be similar in the case of a uniform scattering medium. To quantify the deviation from such behavior, we define an anomaly parameter (A_{DM}) as

$$A_{\text{dm}} = \frac{(\nu_{d_1}/\nu_{d_2})_{\text{observed}}}{(\nu_{d_1}/\nu_{d_2})_{\text{expected}}}, \qquad (7)$$

where ν_{d_1} and ν_{d_2} are the decorrelation bandwidths of pulsars compared for anomaly. The expected values are for a given model of the scattering medium. In the absence of any prior information, we compute the expected values for a uniform scattering medium. For this, we assume that the power spectrum of density fluctuations has a Kolmogorov form, and we consider standard thin-screen scattering models. We also assume that the dependence of scattering with DM is in a similar form to that of distance. Since the parameter A_{dm} quantifies the relative anomaly, it also has the advantage that it is less sensitive to any model-dependent constants related to assumptions made about scattering screen geometries. We define this parameter to be

FIG. 5.—Plot of $\overline{C_n^2}$ against pulsar distance estimates. The upper limit shown by the downward arrow is for the pulsar PSR B0950+08.

always above unity. That is,

$$\text{if } A_{\text{dm}} < 1 , \quad \text{then} \quad A_{\text{dm}} = \frac{1}{A_{\text{dm}}} . \quad (8)$$

Although we lose the information regarding the sense of the anomaly here, it has the advantage that, when averaged over different directions of the sky, anomalies of opposite sense do not cancel each other. This means the parameter will have significant values only when scattering anomalies are consistently present in several directions. The parameter will have unity magnitude in the case of a uniform medium or a spherically symmetric, nonuniform medium in the solar neighborhood. The A_{dm} values are binned over DM interval 3 pc cm^{-3} to compute the average anomalies. The bins are overlapped to include all possible pairs of pulsars in the analysis. A plot of the anomaly parameter against DM is shown in Figure 7a, where the expected values are calculated for a uniform scattering medium with $\overline{C_n^2} \approx 0.2 \times 10^{-4}$ m$^{-20/3}$. It shows a systematic variation where the strength of anomaly decreases with DM. The parameter converges to a value quite close to unity, at DM ~ 13 pc cm^{-3}.

A similar anomaly parameter can be defined for pulsars with comparable distances. Because of the relatively larger uncertainties involved with distances, we consider pulsars differing by $\lesssim 30\%$ in their distance estimates for comparison for anomalous scattering. The anomaly values are binned over a distance range of 200 pc and overlapped to include all possible pairs of pulsars. The anomaly parameter is plotted against distance in Figure 7b. As in the case of DM, a systematic trend is seen with increasing distance, and the magnitude of anomaly converges to a value close to unity, at about $D \sim 700$ pc.

The main implications of these anomaly curves are the following:

1. The relative anomaly technique we used would not have given any meaningful results in the case of spherically symmetric density structures for the solar neighborhood. The anomaly curves, therefore, imply a structure that is highly asymmetric relative to the location of the Sun.

2. The strengths of anomalies are considerably larger at lower DMs ($\lesssim 10$ pc cm^{-3}) and at smaller distances ($\lesssim 600$ pc), and they converge to values quite close to unity at higher values of DM or D. This reaffirms a local origin for the scattering anomalies.

3. Since the anomalous scattering effects, to first order, are confined within a region $\lesssim 500$ pc, they are likely to be connected to a large-scale Galactic structure, such as the Local Bubble.

4. MODELING THE STRUCTURE OF THE LISM

We try to explain our observations in terms of inhomogeneities in the distribution of electron density fluctuations in the LISM. We assume that these density fluctuations are distributed in the form of a large-scale coherent structure. Our model has to account for (1) the enhanced scattering observed for nearby pulsars (Fig. 6) and (2) scattering anomalies and their observed systematic trends with DM and distance (Fig. 7). We consider different types of density structures and examine the viability of each of them in explaining the present observations. As a result of the limited number of measurements, we restrict ourselves to the simplest possible models with as few free parameters as possible.

The model has to be specified by parameters characterizing its size, location, and density fluctuations. We model the structure as a simple ellipsoid, the size of which is parameterized in terms of three semimajor axes, a, b, and c (Fig. 11), where a and b are in the Galactic plane and c is in a plane perpendicular to the Galactic plane. The center of the structure is at an offset r_c from the Sun, toward the direction (l_c, b_c). The scattering strengths are specified by C_n^2 values. The number of C_n^2 parameters would vary depending upon the number of distinct scattering components in the model. Even the simplest possible model will have to be specified by a minimum of eight free parameters, and it may not be possible to determine all of them uniquely from the present observations.

A χ^2 analysis to determine the best-fit parameters of the model is not practicable because of the limited number of
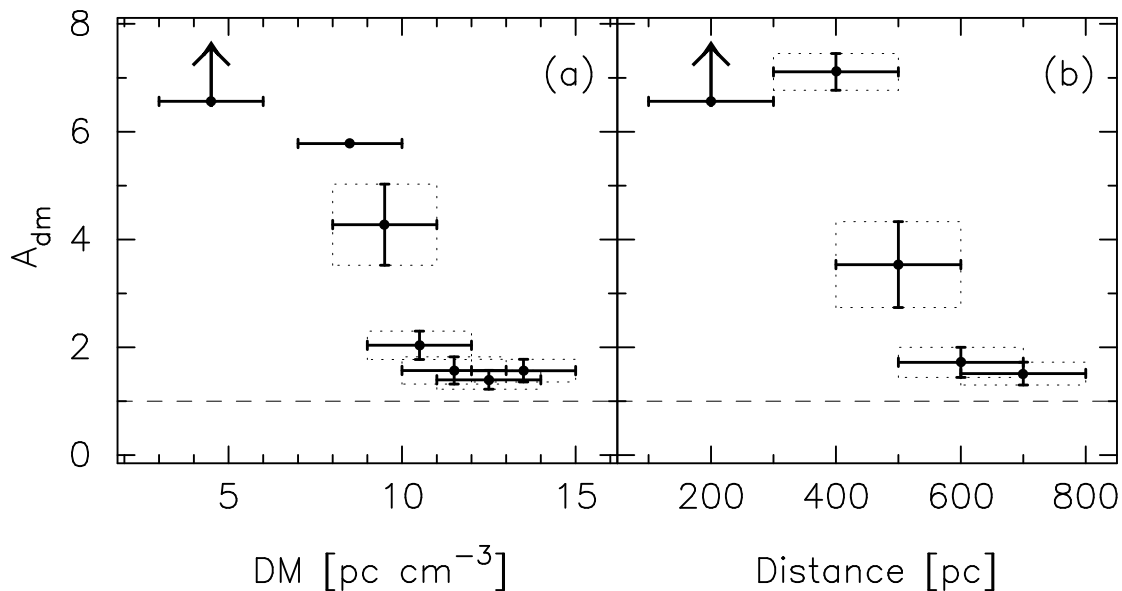

FIG. 7.—Anomaly curves: plots of the anomaly parameter A_{DM} computed (a) for similar DMs and (b) for similar distances. The dashed line is the expected curve in the case of a uniform medium or a spherically symmetric density structure for the solar neighborhood.

measurements. Therefore, we have followed an optimization procedure in which the parameters of the model are adjusted to get the best agreement with the observations. We first assume some initial values for the model parameters, largely based on X-ray, UV, and H I studies of the LISM. Scattering strengths (C_n^2 values) are assumed, depending on the nature of the model considered. We then estimate predicted values of v_d for the observed pulsars, using the method described below. From these, the anomalies expected for the model (A_{dm}^m) and the ratios of the observed decorrelation bandwidths ($v_{d,obs}$) to their predicted values ($v_{d,exp}$) are computed to examine the agreement between the observations and the model predictions. We introduce two quantities, ϵ_A and ϵ_B, that are similar to χ^2 as quantitative measures of the agreement, which are given by

$$\epsilon_A = \frac{1}{N_A} \sum \left[\log (A_{dm}^m) \right]^2 , \qquad (9)$$

$$\epsilon_B = \frac{1}{N_P} \sum \left[\log \left(\frac{v_{d,obs}}{v_{d,exp}} \right) \right]^2 , \qquad (10)$$

where N_A is the number of anomaly ratios and N_P is the number of pulsars. The log scale has been chosen to give equal weight to discrepancies that are below and above unity while computing ϵ_A and ϵ_B. In the first iteration, the free parameters are individually varied over a wide range (0.1–5 times the initial values for a, b, c, r_c, $C_{n,in}^2$, and $C_{n,out}^2$; $0°$ through $360°$ for l_c and $-90°$ through $90°$ for b_c) and are set to values for which ϵ_A and ϵ_B are found to be minimum. The above procedure is repeated iteratively until the quantities ϵ_A and ϵ_B reach minimum values that do not vary significantly. For each iteration, the starting values for the parameters used are the results from the previous iteration and the parameters are varied on a finer grid than in the previous iteration.

To compute the predicted decorrelation bandwidth from our multicomponent scattering model, we use the following technique: first, we note that, for a homogeneous scattering medium, the decorrelation bandwidth is related to the strength of scattering by the relation

$$v_d \propto \frac{1}{D} \left(\int_0^D C_n^2(z)\, dz \right)^{2/(2-\alpha)} , \qquad (11)$$

where the proportionality constant is $(A_\alpha f_{obs}^\alpha)^{-1}$. Our models can be treated as inhomogeneous media consisting of multiple components of different scattering strengths, located at different points along the lines of sight. Since the decorrelation bandwidth is essentially determined by path-length differences of scattered rays, contributions from $C_n^2(z)$ to it need to be appropriately weighted in such a way that scattering regions near the source or the observer produce smaller path-length differences than those that are midway. Cordes et al. (1985) have discussed this aspect in detail and, following their work (eq. [8] of Cordes et al. 1985), for the case of a multicomponent medium, equation (11) can be rewritten as

$$v_d \propto \frac{1}{D} \left[\int_0^{D_1} \frac{z}{D} \left(1 - \frac{z}{D} \right) C_{n,1}^2(z)\, dz \right.$$

$$\left. + \int_{D_1}^{D_2} \frac{z}{D} \left(1 - \frac{z}{D} \right) C_{n,2}^2(z)\, dz + \cdots \right], \qquad (12)$$

where the subscripts 1, 2, ... on C_n^2 denote different components, with medium 1 extending from zero to D_1, medium 2 from D_1 to D_2, and so on. D_1, D_2, ... are computed along the lines of sight of the observed pulsars for a given geometry of the model, and v_d values are estimated by using the model values of $C_{n,1}^2$, $C_{n,2}^2$, ... from which we compute the anomaly ratios, as discussed earlier. The electron density spectrum in the ISM is generally believed to be Kolmogorov. The observations available at present cannot estimate the spectral shape in different components of the ISM. In the absence of any other information, we assume a Kolmogorov density spectrum for all components, and various components of our model are characterized by their respective C_n^2 values.

4.1. Two-Component Models

We have considered two classes of models, viz., two-component and three-component models. Different models that are treated by us under these two classes are listed in Table 3. Since it is believed that the solar system resides in a low-density cavity (Cox & Reynolds 1987) called the Local Bubble, the simplest structure we have considered is a "cavity," where the solar neighborhood has a deficiency of scattering material (i.e., lower magnitudes of electron density fluctuations) compared to the ambient ISM. This model is consistent with the general belief that rms electron density $\Delta n_e \propto n_e$. This is referred to as model I(a). It is basically a two-component model, scattering geometry of which is shown in Figure 8a. The density fluctuations (or, equivalently, the strengths of scattering) of the inner and the outer media are represented by $C_{n,in}^2$ and $C_{n,out}^2$. The ambient medium is considered to be the normal ISM, which is known to have a strength of scattering that varies with z-height (Cordes et al. 1988), and we adopt a scale height $z_o \approx 500$ pc for $C_{n,out}^2(z)$. We assume that C_n^2 is uniformly
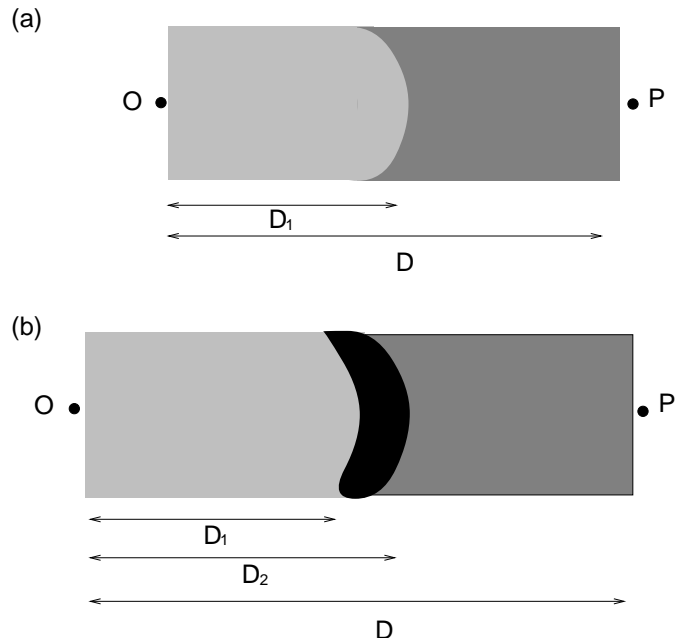
(a)

(b)

FIG. 8.—Schematics showing the scattering geometries of different models. O is the location of the observer and P is that of pulsar. The distribution of C_n^2 along the line of sight is shown through the gray-scale representation, where darker regions correspond to larger values. (a) is for model I(a), and (b) is for model II(a).

<div align="center">TABLE 3</div>
<div align="center">MODELS FOR LOCAL SCATTERING STRUCTURE</div>

Class	Model	Description	ϵ_A (DM)	ϵ_A (D)	ϵ_B	Remark
Two-component	Model I(a)	Cavity of lower density fluctuations $C_{n,\text{in}}^2 < C_{n,\text{out}}^2$	0.0937	0.0293	0.3543	Fails to explain the observations
	Model I(b)	Cavity of higher density fluctuations $C_{n,\text{in}}^2 > C_{n,\text{out}}^2$	0.0485	0.0442	0.2146	Fails to explain the observations
Three-component......	Model II(a)	Shell of enhanced density fluctuations $C_{n,\text{sh}}^2 \gg C_{n,\text{in}}^2$ $C_{n,\text{sh}}^2 \gg C_{n,\text{out}}^2$	0.0604[a] 0.1257[b]	0.0158[a] 0.0172[b]	0.1429[a] 0.1092[b]	Reasonable agreement
	Model II(b)	Similar to Model II(a), with an additional feature of $|z|$-dependent scattering for the shell $C_{n,\text{sh}}^2(z)$; has a scale height $z_d \sim 135$ pc	0.0099[a] 0.0191[b]	0.0073[a] 0.0109[b]	0.1189[a] 0.0779[b]	Best agreement

[a] For the solid enclosure shown in Fig. 11.
[b] For the dashed enclosure shown in Fig. 11.

distributed inside the cavity in the absence of any prior information regarding the same. The optimization procedure described earlier has been carried out, and we find this model fails to reproduce the observed scattering anomalies and does not give rise to enhanced scattering strengths for nearby pulsars (Figs. 9c, 9d, and 10a).

Although it is generally assumed that $\Delta n_e \propto n_e$, the exact relation is not obvious, and there can be exceptions to this. Therefore, the possibility of existence of a low-density region with larger magnitudes of electron density fluctuations cannot be totally ruled out. We have investigated such a scattering structure, referred to as model I(b) in Table 3, in which the solar system is embedded in a region of relatively larger magnitude of density fluctuations than the ambient ISM ($C_{n,\text{in}}^2 > C_{n,\text{out}}^2$). Such a structure, however, would fail to explain the low scattering strength observed with the closest pulsar, PSR B0950+08. Since there are not many pulsars with low scattering strengths, we examined the viability of this model as well. The model, however, did not reproduce the observed anomalies, and its comparison with observations is shown in Figures 9e, 9f, and 10b.

4.2. Three-Component Models

The second class of models we have considered are three-component models, where we have added to the model I(a) a shell of enhanced scattering. Such a structure is plausible, since supernova-produced bubbles are expected to have dense shells surrounding them. Such a structure, referred to as model II(a) in Table 3, can give rise to both the low scattering strength for the closest pulsar and enhanced scattering strengths for nearby pulsars. Enhanced scattering can be expected for pulsars outside the shell boundary. This will have a systematic decreasing trend with distance, since the relative contribution from the shell to the total scattering decreases with distance. To parameterize this model, in addition to the parameters described above, we also need to consider parameters characterizing scattering from the shell. To simplify the modeling procedure, we consider the case of a "thin" shell, with a thickness much smaller than pulsar distances ($d \ll D$). The scattering strength due to the shell material is specified by its density fluctuation parameter $C_{n,\text{sh}}^2$, and we assume that density fluctuations have a uniform distribution within the shell region. To simplify the

model, we characterize the scattering from the shell by the integral of $C_{n,\text{sh}}^2$ over the thickness, thereby requiring only one free parameter for the shell. We also assume that this dense shell has much higher levels of density fluctuations than both the interior of the bubble and the ambient ISM. The scattering geometry in this case is shown in Figure 8b. We find the shell structure succeeds, to some extent, in reproducing some of the observed scattering anomalies, and we get a reasonable agreement with the observed anomaly curves (Figs. 9g, 9h, and 10c). Though there is significant improvement compared to earlier cases of simpler structures, as can be seen from their ϵ_A and ϵ_B values, there exists some disagreement that can be seen as significant deviations of some of the anomaly values from unity (Figs. 9g–9j) and discrepancies in v_d values of some pulsars (Figs. 10c and 10d).

On carefully examining the predictions of model II(a), we find the agreement with the observations is poor in the case of pulsars at larger z-heights. To account for this, we assume that the strength of scattering from the shell decreases with $|z|$, as in the case of ambient ISM. This is a variant of the previous model and is called model II(b). If we presume that both the cavity and its shell boundary have formed out of rather smoothly distributed Galactic disk components, it is reasonable to assume that the density fluctuations in the shell have characteristics similar to that of density variations of the disk component. We assume a scale height $z_d \sim 135$ pc for $C_{n,\text{sh}}^2(z)$, which is the scale height of the neutral gas density variations in the Galactic disk component (Bloemen 1987). This would lead to substantial changes in the magnitude of density fluctuations with $|z|$ and can give rise to relatively weaker scattering strengths for pulsars at larger z-heights than that which is caused by the earlier model. We carried out the optimization procedure to determine the best parameters of this model and find that it reproduces the observed anomalies quite well. The excess scattering (v_d ratios) is also better accounted for. The agreement between the observed and predicted anomalies is shown in Figures 9k, 9l, and 10e and is the best among different models considered by us. Note that the anomaly values A_{dm}^m and $v_{d,\text{obs}}/v_{d,\text{exp}}$ are quite close to unity, suggesting the success of the model in explaining the present observations. In addition, residual anomalies are randomly
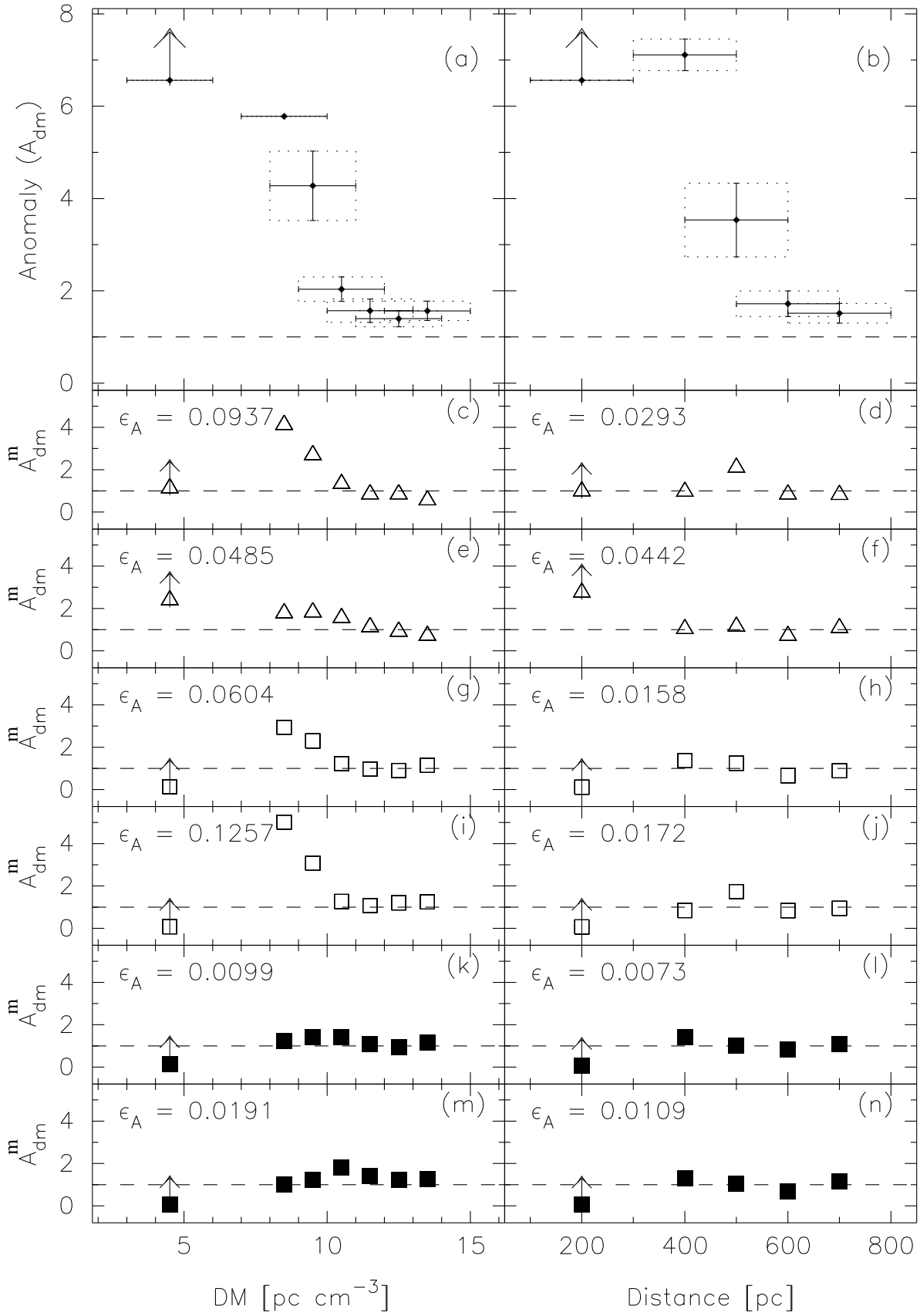
FIG. 9.—Agreement between the observations and the predictions of various models, shown in terms of plots of their A_{DM} values against DMs and the distances. The top panels, (a) and (b), are for a uniform scattering medium; (c) and (d) are for model I(a), and (e) and (f) for model I(b). Panels (g)–(j) are for model II(a) for the two possible geometries shown in Fig. 11, and (k)–(n) are for model II(b) for the two geometries.
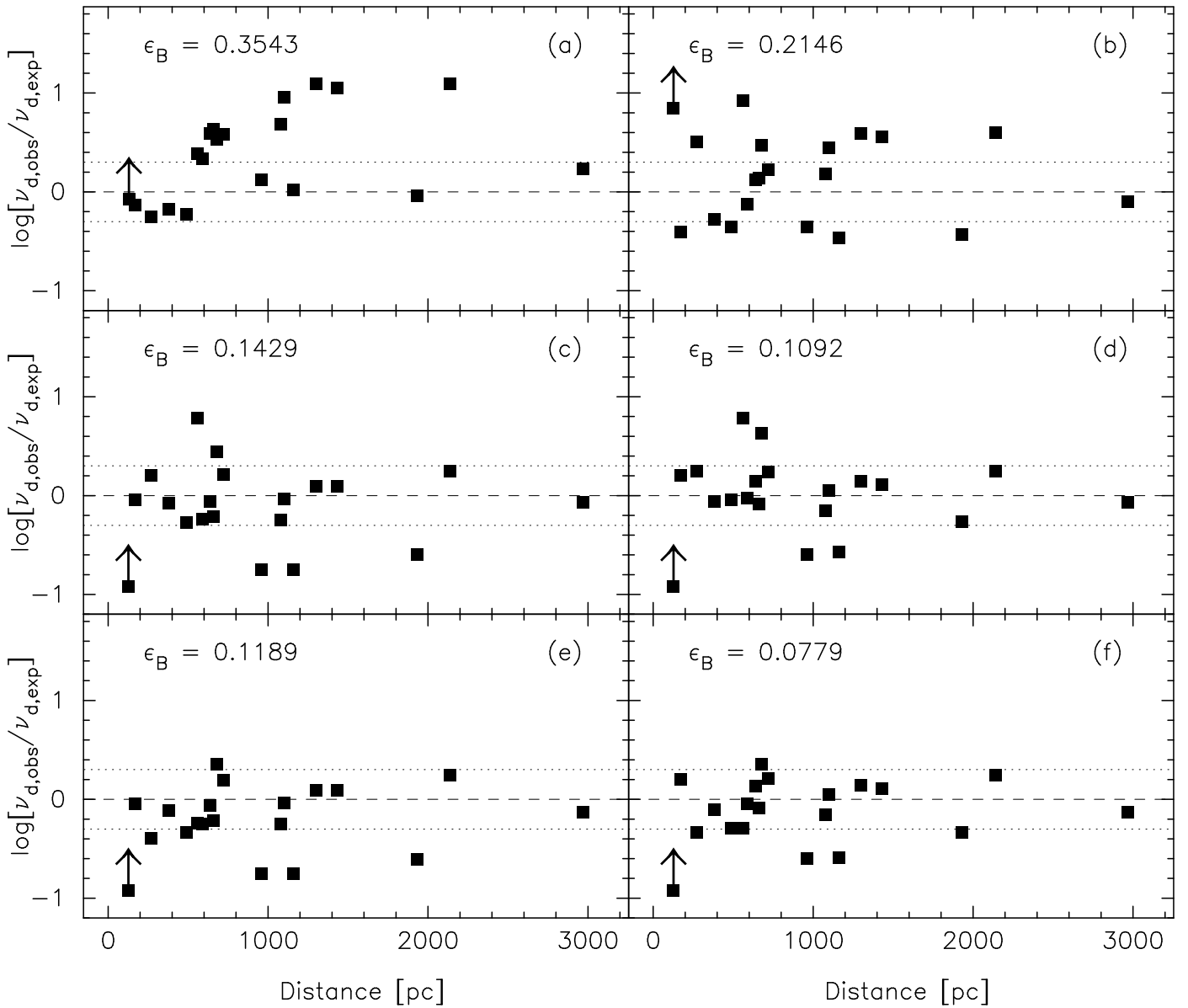
FIG. 10.—Ratios of the observed decorrelation bandwidths ($v_{d,\mathrm{obs}}$) to their values predicted by various scattering models ($v_{d,\mathrm{exp}}$). Panel *a* is for model I(a), and panel *b* is for model I(b); (*c*) and (*d*) are for model II(a) and for the solid and dashed geometries of Fig. 11, respectively; (*e*) and (*f*) are for model II(b) for the two geometries. The dotted lines correspond to a discrepancy of a factor of 2.

TABLE 4

GEOMETRICAL PARAMETERS AND SCATTERING PROPERTIES OF THE BEST-FIT MODEL

Model Parameter	Value
Physical dimensions of the ellipsoid (semimajor axes *a*, *b*, and *c*) (pc):	
Perpendicular to the Galactic plane (NGP-SGP cut)	$270 < c < 330$
In the Galactic plane (0°–180°)[a]	$60 < a < 75$
In the Galactic plane (90°–270°)[a]	$60 < b < 75$
Location of the center of the ellipsoidal shell:	
Galactic longitude (deg)	$215 < l_c < 240$
Galactic latitude (deg)	$-20 < b_c < 20$
Offset from the Sun (pc)[a]	$35 > r_c > 20$
Strengths of scattering (C_n^2) of different components:	
Inner cavity (m$^{-20/3}$)	$10^{-4.70} < \overline{C_n^2} < 10^{-4.22}$
Shell material (with thickness *d*) (pc m$^{-20/3}$)	$10^{-0.96} \leq \int_0^d C_n^2(l)dl < 10^{-0.55}$
Outer ISM (m$^{-20/3}$)	$\overline{C_n^2} < 10^{-3.30}$

[a] Smaller values of *a* and *b* require a larger value of r_c to reproduce the results.
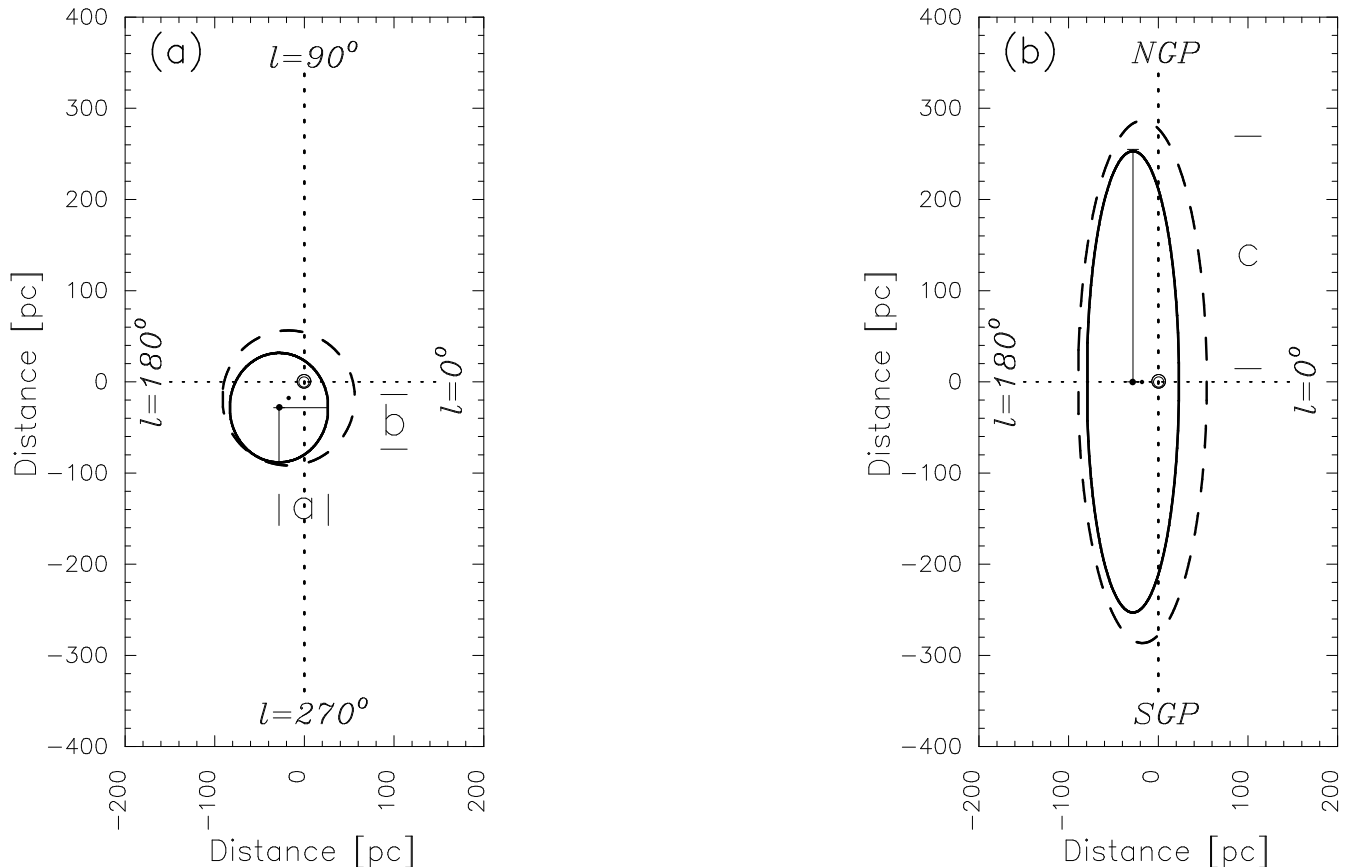
FIG. 11.—Geometry of the best-fit model, model II(b), for the local scattering structure. Panel a is the section in the Galactic plane, and panel b is the section along a plane perpendicular to the Galactic plane and passing through the north and the south Galactic poles. The solid enclosure is for $r_c \sim 35$ pc, $a \sim 60$ pc, and $b \sim 60$ pc, and the dashed one has $r_c \sim 20$ pc, $a \sim 75$ pc, and $b \sim 75$ pc.

placed with respect to zero, thereby ruling out any systematic trends. The geometrical parameters and the scattering properties of the local scattering structure inferred from the model are listed in Table 4. The suggested geometry is schematically shown in Figure 11 (*solid curve*) as cuts through the Galactic plane (Fig. 11*a*) and along a plane perpendicular to $b = 0°$ and passing through the Galactic poles (Fig. 11*b*).

A unique determination of all parameters has not been possible from the present observations. However, it has enabled us to get some useful insights on a possible scattering structure and derive reasonable constraints on its size and the location and strength of scattering. Note that the constraints on the semimajor axis c, the direction (l_c, b_c), and the integrated strength of scattering from the shell are rather tight, since these parameter values are critical in determining the scattering anomalies. However, we have not been able to derive similarly tight constraints on the rest of the parameters. Our present sample does not consist of many pulsars whose scattering properties are predominantly determined by either the cavity only or the ambient ISM only; therefore, our constraints on their strengths of scattering ($\overline{C}_{n,\text{in}}^2$ and $\overline{C}_{n,\text{out}}^2$) are not very tight. Also, the present measurements do not allow us to put unique constraints on the size in the Galactic plane (semimajor axes a and b) and the offset to the center (r_c) from the Sun. Our results can also be explained by a structure that is relatively bigger ($a \approx b \sim 75$ pc), if its center is located nearer to the Sun ($r_c \sim 20$ pc). This is shown as the dashed geometry in

Figures 11*a* and 11*b*. It can be stated that intermediate structures within $35 > r_c > 20$ pc, $60 < a < 75$ pc, and $60 < b < 75$ pc are also equally possible, with an asymmetry that becomes less pronounced with the increase of size. It is not possible to resolve this ambiguity using the present measurements alone.

5. DISCUSSION

5.1. *Successes and Limitations of the Model*

We have attempted to explain our observations by considering an inhomogeneous distribution of electron density fluctuations in the LISM. We have confined ourselves to the simplest possible density structures required to reproduce the observed trends. Simple models in which the solar neighborhood has an enhanced or a reduced scattering strength relative to the ambient medium fail to explain our observations. We need a three-component medium consisting of a shell of enhanced scattering surrounding the solar neighborhood that has lower scattering strength compared to the normal ISM. The salient features of our model, shown schematically in Figure 11, are as follows:

1. The scattering structure has an ellipsoidal morphology, with a size in the plane perpendicular to the $b = 0°$ plane being about 5 times larger than in the Galactic plane.

2. The Sun is located away from the center of the structure but must be well inside of it.

3. The density fluctuations in the shell are much larger than those in the interior and in the normal ISM. For

nearby pulsars, the shell contributes substantially to the scattering, as compared to the cavity and the normal ISM.

4. There is a suggestion that the strength of scattering of the shell decreases with the height above the Galactic plane.

5. The strength of scattering in the inner cavity is about 5 times lower than that of the normal ISM.

This three-component model is able to reproduce a number of the observed trends in the data. The model accounts for the observed scattering anomalies with good success (Figs. 9k–9n). It also accounts for the enhanced scattering of nearby pulsars and reproduces the observed trend in the variation of the decorrelation bandwidths with distance (Figs. 10e and 10f). From our model, we are able to obtain constraints on the geometrical parameters and the scattering properties of the structure (Table 4).

We have investigated only the simplest models and cannot rule out the possibility of better fits with more complex models. Our modeling is constrained by the limited number of pulsars used for probing the LISM. The model has nine free parameters, and the present data are not good enough to constrain all of them equally well. We are able to put tight constraints on the size along the plane perpendicular to the Galactic plane, the direction of the center, and the strength of scattering of the shell (Table 4). However, the strengths of scattering of the cavity and the ambient medium are poorly constrained. Also, we are unable to distinguish between a small, highly asymmetric structure and a less asymmetric but bigger structure (Fig. 11). Intermediate structures within $35 > r_c > 20$ pc, $60 < a < 75$ pc, and $60 < b < 75$ pc are also consistent. However, it is clear that the smaller structures need to be more asymmetric. We cannot constrain the thickness of the shell, because there seem to be no pulsars situated in the shell, but can only estimate the integrated strength of scattering.

5.2. Implications for the Electron Density Distribution in the LISM

The electron density distribution in the LISM can be studied using the dispersion properties of nearby pulsars. However, a detailed study is not feasible at present because independent distance estimates are available for only two of our pulsars (Table 1). The pulsar, PSR B0950+08, that has a parallax distance ≈ 130 pc (Gwinn et al. 1986) is located in our model, within the cavity. Its DM implies $n_e \approx 0.02$ cm^{-3}, which is about 4 times larger than its value based on the model given by Snowden et al. (1990) for the distribution of the soft X-ray background.

Scintillation measurements provide us with information on the distribution of electron density fluctuations. However, the apparent lack of understanding about the exact relations between the scattering strengths and other properties of the medium prevents us from deducing the n_e distribution directly from that of density fluctuations. The presence of an inhomogeneous medium is likely to be more prominent in scintillation, owing to the nonlinear relation of scintillation properties to the electron density. Therefore, even the regions of density enhancements that do not contribute significantly to the dispersion are likely to be detectable through their scintillation effects. The Vela pulsar (PSR B0833−45) is a good example, where a density enhancement of a factor of 5 and a C_n^2 enhancement of a factor of $\gtrsim 100$ are known to exist (Rickett 1977). Also, unlike disper-

sion, scintillation effects are sensitive to the locations of the scattering regions and, therefore, are useful for inferring the locations of regions of enhanced scattering. Thus, the information provided by the dispersion and the scintillation measurements appear to be complementary and can enable us to derive much better insights on the n_e distribution in the LISM.

It is generally believed that the regions of enhanced electron densities are also the sites of enhanced electron density fluctuations ($\Delta n_e \propto n_e$; Rickett 1970). Therefore, an ellipsoidal shell structure for the density fluctuations would imply the existence of a dense electron density shell surrounding a low electron density cavity. Our simplified model constrains only $\int C_n^2 \, dl$ and not the thickness of the shell, which is essential for determining the electron density in the shell. If we assume that $C_n^2 \propto n_e^2$, our observations imply a density contrast ~ 10–20 times between the shell and the ambient ISM, in the case of a thin shell ($d \sim 1$ pc), and ~ 5–8 times for ~ 10 pc thick shell. The pulsar PSR B0823+26 lies well outside the bubble in our model and has a parallax distance of ≈ 380 pc (Gwinn et al. 1986). The shell is located at ~ 100–110 pc in the direction of this pulsar. If we assume $n_e \approx 0.02$ cm^{-3} for the bubble interior and a canonical n_e of ≈ 0.025 cm^{-3} for the outer medium, this would mean a density contrast of ~ 30 for an approximately 10 pc thick shell. This is, however, about 3–6 times larger than that which is estimated from our model. Nevertheless, a possible density enhancement is indicated.

The distance estimates used in our analysis are based on the model (Taylor & Cordes 1993) that does not take into account a possible inhomogeneous distribution of n_e in the LISM. In order to examine the role of the LISM in determining the pulsar distances, we reestimated them by incorporating a shell density structure for the LISM. We studied the cases of both the thin and the thick shells with the expected density contrasts estimated from the parameters of our scattering structure. For these calculations, we have assumed $n_e \approx 0.02$ cm^{-3} for the inner cavity and the canonical n_e of ~ 0.025 cm^{-3} for the ambient ISM. We have also taken into consideration smooth variations of the densities in the shell and in the ambient medium with z-height. Here we assumed an exponential decrease, with a scale height ~ 500 pc for n_e in the ambient medium and a Gaussian with a scale height ~ 125 pc for n_e in the shell.

In the case of the thin shell with a density contrast of 10, we find the new distances to be similar to their presently available estimates for most pulsars (Fig. 12a). Barring a few anomalous ones (PSR B0823+26, PSR B2016+28, PSR B1508+55, and PSR B0919+06), the new distances typically differ by 10%. For a higher density contrast of 20, the difference is only marginal. In the case of the thick shell, dispersion due to the shell becomes more significant, but it is still not enough to produce considerable changes in the distance estimates. Discrepancies between the two distances are larger for a thick shell, and they differ typically by 25% for a 10 pc thick shell with a density contrast of 8 (Fig. 12b). Therefore, the density enhancements implied by our model do not alter the distance estimates to our pulsars significantly. This gives an ex post facto justification of our analysis procedure, where we have used the available distance estimates, and also suggests that a linear relation between the DMs and the distances is a reasonable approximation in the LISM, despite its seemingly inhomogeneous nature of n_e distribution. However, to establish this firmly,
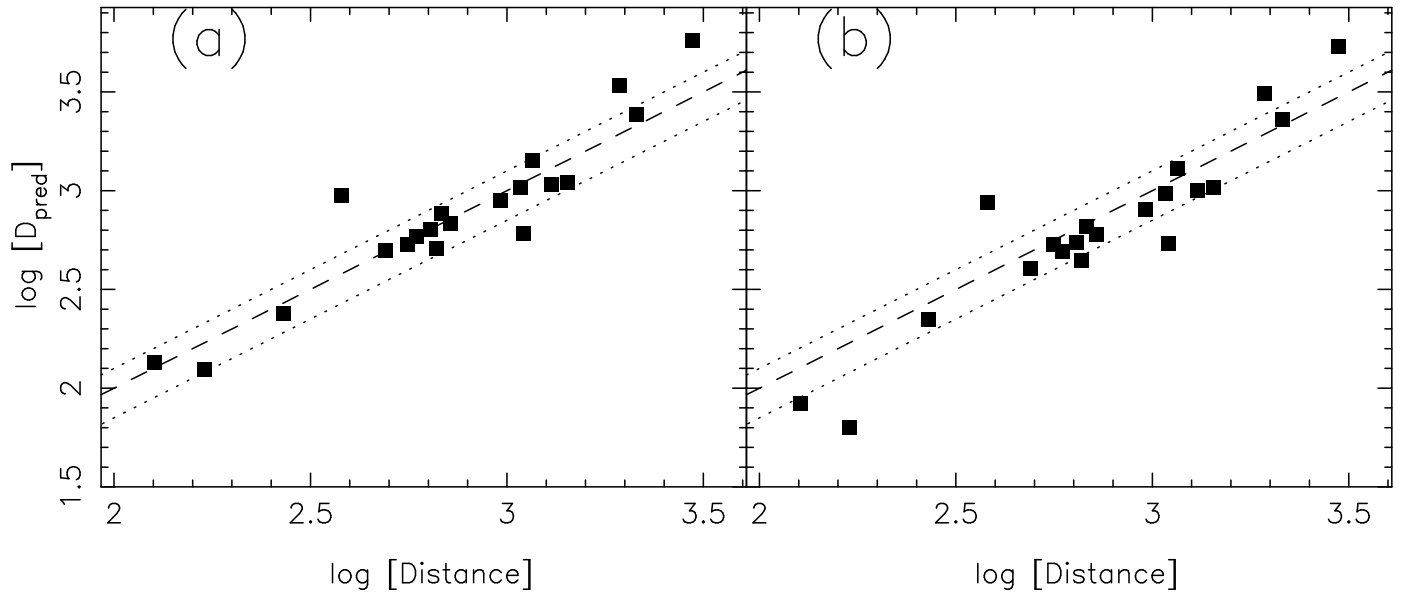
FIG. 12.—Predicted distance estimates (D_{pred}) of pulsars for a shell density structure plotted against presently available distance estimates. Panel a is for the thin (thickness ~ 1 pc) shell of density contrast 10, and panel b is for the thick (~ 10 pc) shell with a density contrast 8. The dashed lines correspond to a discrepancy of 30%.

we need more accurate distance estimates for local pulsars than are available from the model of Taylor & Cordes (1993).

5.3. Possible Tests of the Present Model

Observations of more pulsars will be useful for further constraining the parameters of our scattering model. The number of local pulsars (within a distance of $\lesssim 1$ kpc) has nearly doubled since we started our observations at ORT as a result of recent pulsar surveys, and forms a large enough sample from which to study the n_e distribution in the LISM. Scintillation measurements of pulsars, however, require long-term observations to get reliable estimates of their strengths of scattering. But there are simpler tests with which to verify the expectations based on our model, and we discuss a few of them here. In particular, it is possible to use some of the recently discovered local pulsars to verify the predictions on their scattering properties. One example in this regard is PSR J1730−2304 ($l \approx 3°1$, $b \approx 6°$), a pulsar located at a close-by distance (~ 510 pc), for which preliminary observations from the ORT show that its enhanced scattering is consistent with model predictions.

In the specific cases of pulsars for which the scattering is due predominantly to the shell, one can treat the scattering, to first order, as resulting from an equivalent thin screen located at the shell. In such cases, it is possible to use some distance-dependent scattering properties to check the predicted locations of the shell boundaries in those directions. A straightforward test is the comparison between the proper motion and scintillation speeds. The former speeds are determined by pulsar distances, whereas the latter speeds also depend on the relative location of the screen (Gupta et al. 1994). The comparison, however, requires a careful analysis, since the scattering geometries of our pulsars are represented by multicomponent, inhomogeneous media.

Pulse broadening resulting from scattering is another property that is sensitive to the nature of distribution of the scattering material along the line of sight and, hence, can be

used to distinguish between the thin screen and the extended screen geometries of scattering (Lyne & Smith 1990; Williamson 1974). The broadening is, however, not significant at 327 MHz for low-DM pulsars and cannot be studied using our data. However, observations at lower frequencies can provide useful information. Some promising pulsars in this aspect are PSR B1929+10, PSR B1133+16, PSR B0823+26, and PSR B2327−20, where a broadening typical of a thin screen can be expected according to our model. In the case of pulsars PSR B1237+25 and PSR B0950+08, broadening features typical of those due to extended media are expected. The observations, however, require high time resolution (~ 0.1 ms) and need to be carried out at observing frequencies $\lesssim 100$ MHz for meaningful results.

The data from observations at 25 MHz (Phillips & Wolszczan 1990) reveal that three of our pulsars—PSR B0823+26, PSR B0834+06, and PSR B0919+06—display pulse shapes with sharp rising edges (Fig. 2 in Phillips & Wolszczan 1990). For these pulsars, according to our model, scattering is predominantly ($\gtrsim 75\%$) due to the shell material; hence, the scattering geometry can be considered to be closer to that of a thin screen, in which case broadening features, characterized by a sharp rising edge followed by an exponential tail, can be expected. Given the signal-to-noise ratio of the profile of PSR B1604−00, such a feature is not apparent, and the pulse shape seems to imply a diffused scattering medium in its line of sight. For this pulsar, our model predicts substantial amounts of scattering due to the shell material as well as the outer ISM; therefore, the scattering geometry can be treated more like that of a "continuous medium," which is in accord with the observed pulse shape. Pulse shapes of PSR B0950+08 and PSR B1133+16 are hard to interpret, since their profiles seem to be changing significantly with the observing frequency and the scattering is low. Leaving out these two pulsars, pulse shapes of the remaining four are consistent with expectations of our scattering model. Further low-frequency observations of nearby pulsars will be useful.

Decorrelation bandwidth is another observable that depends on the location of the scattering screen. For a given location of the screen, it is essentially determined by the angular broadening of the scattered rays. Therefore, simultaneous measurements of these two quantities will be useful for deriving the effective location of the scattering screen; for pulsars with predominant scattering from the shell, this essentially means the location of the shell. Angular broadening measurements, therefore, also form suitable techniques for testing our scattering model. Although such observations have been reported recently (Gwinn, Bartel, & Cordes 1993) for 10 pulsars, the scattering disks of four common pulsars—PSR B1919+21, PSR B1929+10, PSR B2016+28, and PSR B2020+28—were unresolved; therefore, interpretation of their angular broadening measurements is uncertain. Pulsars which show relatively much higher levels of scattering, such as PSR B0823+26, PSR B1133+16, and PSR B2327−20, form some of the suitable candidates for further observations.

5.4. Comparison with Other Studies of the LISM

Snowden et al. (1990) have derived the three-dimensional geometry for the X-ray–emitting cavity using their "displacement model" technique. They have considered two specific models, which are the cases of a cavity formed (1) by simply removing the material and (2) by sweeping out the material to form a shell at the edge of the emission region. The local scattering structure deduced by us has a shell morphology and favors this second model, if we assume $\Delta n_e \propto n_e$. The size of our ellipsoidal shell is quite similar to their larger cavity (Figs. 6 and 7 in Snowden et al. 1990), suggesting a connection between the scattering structure and the X-ray cavity. The inferred cavity is much more extended away from the Galactic plane, with a striking asymmetry between the northern and the southern Galactic hemispheres (Cox & Snowden 1986; Snowden et al. 1990). The scattering structure derived by us also has a morphology that is much more extended away from the Galactic plane and, therefore, resembles that of the X-ray cavity. However, an asymmetry between the two hemispheres has not been clearly established for our scattering structure (see the constraints on the location of the center given in Table 4). The present data are not good enough to draw a firm conclusion on this. Also, we find that the Sun needs to be significantly off-centered within the structure, a property that was not clearly established in the X-ray studies, owing to regions of data with non–X-ray contamination and of poor spatial coverage.

Warwick et al. (1993) studied the properties of EUV source population using the data from ROSAT. Their simple model of a spherical bubble of average radius $\sim 100 \pm 25$ pc, centered at the Sun, with an interior gas density ~ 0.05 cm^{-3}, can account for the observed characteristics of the global source counts. The bubble radius derived from their analysis and the radius of an equivalent sphere for our scattering structure are comparable, suggesting a zeroth-order consistency between the two. They also studied the spatial distribution of the sources and identified anomalous regions with a deficit or an excess compared to the global average, which they interpreted in terms of deviations from their "fiducial" bubble model. In particular, they estimated the distances to the bubble boundaries toward some specific regions where prominent features

were seen. They suggested the existence of a relatively nearby (~ 10 pc) absorbing wall toward the general direction of the Galactic center to explain an observed deficiency of a factor of 5 in the number of sources. A close-by location (~ 20 pc) of the shell in this direction is expected from our scattering structure, too. An excess of a factor of 2 was seen in the southern part of Galactic quadrant III ($l \approx 200°$, $b \approx -30°$), from which they inferred a bubble extent of ~ 100 pc, which is comparable to the distance to the shell boundary estimated from our model ($\sim 100–110$ pc) in this direction. Also, from an excess in the northern sky ($l \approx 120°$, $b \approx 45°$), it was suggested that the bubble extends well beyond ~ 120 pc toward this region. Given the uncertainties of our model parameters, a bubble extent as large as ~ 80 pc can be expected in this direction. Therefore, it appears that the morphology and the size of our scattering structure are in broad agreement with those of the UV bubble, suggesting a possible connection between the distributions of electron density fluctuations and that of absorbing gas in the LISM.

Hajivassiliou (1992) has proposed an ellipsoidal envelope of high plasma turbulence around the Sun to explain the large-scale features seen in the turbulence map derived using angular source size measurements from an interplanetary scintillation (IPS) survey made at 81.5 MHz (Fig. 1 in Hajivassiliou 1992). This interpretation requires the Sun to be lying at the edge of the envelope, in the direction $l \approx 30°$, to explain the observed directional anisotropy of the turbulence parameter. Although the scattering structure deduced by us has a similar morphology, there is little agreement on other properties, such as the size, location, and strength of scattering. The estimates on the size of our scattering structure are much larger than that of the ellipsoidal envelope suggested from the IPS data. The morphology and the size of the envelope were based on the X-ray data (Cox & Snowden 1986), where radii of ~ 150 pc and ~ 45 pc were typical for the ellipsoidal sections perpendicular to and in the Galactic plane, respectively, which are much smaller than those inferred from our data (radii of ~ 250 pc and ~ 60 pc on these planes; Fig. 11). Also, we find in our model that the Sun needs to be located well inside the shell structure (offset $\sim 20–35$ pc) to explain the observed scattering anomalies of pulsars. Considerable discrepancy exists in the estimates of strengths of scattering of the shell, where the integrated strength of scattering constrained from our observations (Table 4) is $\sim 2–5$ times smaller than that required to explain the IPS data. Furthermore, in our model, scattering due to the shell decreases with height above the Galactic plane and becomes an order of magnitude lower at $|b| \approx 90°$, something that has not been considered by Hajivassiliou (1992).

Studies of the distribution of the neutral hydrogen in the LISM (Frisch & York 1983; Paresce 1984) reveal the existence of a large region of about 100 pc surrounding the Sun that is virtually devoid of neutral hydrogen (density $n_{\rm H\,I} \lesssim 0.1$ cm^{-3}). This "void" has an opening in Galactic quadrant III (Fig. 4 in Paresce 1984). The Sun seems to be located away from the center of this void, and a boundary, defined as the distance where the column density of neutral hydrogen becomes $\sim 10^{19}$ cm^{-2} (Cox & Reynolds 1987), is fairly close by in Galactic quadrant I (toward $l \approx 45°$), whereas it is about 50 pc away from the Sun in quadrants II and IV. It is interesting to note that, in quadrants I, II, and IV, the morphology of our scattering structure has a broad

resemblance to that of this H I void. Also, our estimates of the bubble boundaries in quadrants I, II, and IV are comparable to those of the H I void. In our model, the bubble region extends to much larger distances in quadrant III. A similar property can be seen in the H I void, suggesting a broad consistency between the two. On the basis of the morphological similarity between the two structures, there appears to exist a probable connection between the interior of our shell structure and the H I void.

In view of the morphological agreement between the X-ray–emitting cavity, the UV bubble, the neutral hydrogen void, and the local density structure from our observations, properties of the large-scale distributions of the neutral and the ionized materials in the Local Bubble can be summarized as follows: The hot gas giving rise to the soft X-ray emission seems to fill the local void of neutral hydrogen. The deficiency of neutral hydrogen enhances the chances of detections of the EUV sources, which is confirmed from the recent observations. Also, the observed properties of EUV sources and their spatial distribution are broadly consistent with the morphology of the void. Lower magnitudes of electron density fluctuations seem to prevail in this region, which is broadly consistent with lower electron densities expected from the displacement model. Our observations also suggest that the bubble region is surrounded by a shell of much higher density fluctuations. This implies a similar structure for the distribution of n_e, which needs to be confirmed.

6. CONCLUSION

For the first time, the structure of the LISM has been modeled using the results from a systematic, long-term pulsar scintillation study. Our analysis, based on the scintillation properties of 20 nearby pulsars, suggests that the large-scale distribution of the ionized material in the solar neighborhood is not uniform. Systematic trends have been seen in the scattering properties of pulsars, which imply a coherent structure of electron density fluctuations in the LISM. The detailed analysis of the observed anomalous scattering effects shows that such a structure is highly asymmetric relative to the location of the Sun. Simple models in which the solar neighborhood has an enhanced or a reduced scattering strength relative to the ambient medium fail to reproduce the scattering anomalies. To explain our observations, we need a three-component scattering medium in which the solar neighborhood is surrounded by a shell of much higher density fluctuations embedded in the normal, large-scale ISM. We are also able to put reasonable constraints on the geometrical and the scattering properties characterizing the size, location, and density fluctuations of such a structure. The shell has an ellipsoidal morphology and is much more extended away from the Galactic plane than in the plane, with radii of ~ 270–330 pc and ~ 60–75 pc for the sections along the Galactic poles and through the Galactic plane, respectively. The Sun is located away from the center by about ~ 20–35 pc. The density fluctuations in the shell are much larger than those in the interior and in the outer region, and there is a suggestion that they decrease with height above the Galactic plane. We also find that the morphology of our scattering structure is similar to that of the Local Bubble known from various earlier studies, based on H I, X-ray, and UV data. The LISM and the distribution of electron density fluctuations in it are likely to be more complex than is suggested by our simplified model, but we hope the present work will serve as a useful framework within which more detailed questions can be addressed.

REFERENCES

Armstrong, J. W., Rickett, B. J., & Spangler, S. R. 1995, ApJ, 443, 209
Bhat, N. D. R., Rao, A. P., & Gupta, Y. 1998a, in preparation
———. 1998b, in preparation
Bloemen, J. B. G. M. 1987, ApJ, 322, 694
Bochkarev, N. G. 1987, Ap&SS, 138, 229
Cordes, J. M. 1986, ApJ, 311, 183
Cordes, J. M., Pidwerbetsky, A., & Lovelace, R. V. E. 1986, ApJ, 310, 737
Cordes, J. M., Spangler, S. R., Weisberg, J. M., & Clifton, T. R. 1988, in AIP Conf. Ser. 174, Radiowave Scattering in the Interstellar Medium, ed. J. M. Cordes, B. J. Rickett, & D. C. Backer (New York: AIP), 180
Cordes, J. M., Weisberg, J. M., & Boriakoff, V. 1985, ApJ, 288, 221
Cordes, J. M., Weisberg, J. M., Frail, D. A., Spangler, S. R., & Ryan, M. 1991, Nature, 354, 121
Cox, D. P., & Reynolds, R. J. 1987, ARA&A, 25, 303
Cox, D. P., & Snowden, S. L. 1986, Adv. Space Res., 6(2), 97
Frisch, P. C., & York, D. G. 1983, ApJ, 271, L59
Gupta, Y., Rickett, B. J., & Lyne, A. G. 1994, MNRAS, 269, 1035
Gwinn, C. R., Bartel, N., & Cordes, J. M. 1993, ApJ, 410, 673
Gwinn, C. R., Taylor, J. H., Weisberg, J. M., & Rawlings, L. A. 1986, AJ, 91, 338
Hajivassiliou, C. A. 1992, Nature, 355, 232
Lyne, A. G., & Smith, F. G. 1990, Pulsar Astronomy (Cambridge: Cambridge Univ. Press)
McCammon, D., & Sanders, W. T. 1990, ARA&A, 28, 657
Paresce, F. 1984, AJ, 89, 1022
Phillips, J. A., & Clegg, A. W. 1992, Nature, 360, 137
Phillips, J. A., & Wolszczan, A. 1990, in Lecture Notes in Physics 362, Low-Frequency Astrophysics from Space, ed. N. E. Kassim & K. W. Weiler (Berlin: Springer), 175
Rickett, B. J. 1970, MNRAS, 150, 67
———. 1977, ARA&A, 15, 479
———. 1990, ARA&A, 28, 561
Roberts, J. A., & Ables, J. G. 1982, MNRAS, 201, 1119
Romani, R. W., Narayan, R., & Blandford, R. D. 1986, MNRAS, 220, 19
Selvanayagam, A. J., Praveenkumar, A., Nandagopal, D., & Veluswamy, T. 1993, Inst. Electron. Telecommunications Engin. Tech. Rev., 10, 333
Smith, F. G., & Wright, N. C. 1985, MNRAS, 214, 97
Snowden, S. L., Cox, D. P., McCammon, D., & Sanders, W. T. 1990, ApJ, 354, 211
Spangler, S. R. 1988, in AIP Conf. Proc. 174, Radiowave Scattering in the Interstellar Medium, ed. J. M. Cordes, B. J. Rickett, & D. C. Backer (New York: AIP), 32
Subramanian, R. 1989, Ph.D. thesis, Indian Inst. Sci.
Swarup, G., et al. 1971, Nature Phys. Sci., 230, 185
Taylor, J. H., & Cordes, J. M. 1993, ApJ, 411, 674
Warwick, R. S., Barber, C. R., Hodgkin, S. T., & Pye, J. P. 1993, MNRAS, 262, 289
Williamson, I. P. 1974, MNRAS, 166, 499